NEARSHORE BATHYMETRY ESTIMATION FROM DRONE VIDEO USING PIV TECHNIQUE

A Thesis

by

SHIH-HENG SUN

Submitted to the Office of Graduate and Professional Studies of
Texas A&M University
in partial fulfillment of the requirements for the degree of

MASTER OF SCIENCE

Chair of Committee,	Kuang-An Chang
Committee Members,	James Kaihatu
	Russell Feagin
Head of Department,	Sharath Girimaji

December 2017

Major Subject: Ocean Engineering

ABSTRACT

This research introduces a novel method to estimate nearshore bottom topography using an unmanned aerial vehicle (UAV), or drone. The UAV was manipulated over the area of interest to film video, and the Particle image velocimetry (PIV) technique was then applied to analyze the video frames in order to retrieve the wave speeds. Under the shallow water conditions, the wave dispersion relation can be simplified in a manner such that when the wave speed is known, the water depth can be inferred. In other words, when wave speed is known, water depth can be inferred. After combining the inferred water depths at multiple points from within the area of interest, the bathymetry was constructed.

To validate the method, individual waves were recorded in the nearshore breaking zone during two trials at Freeport, Texas, USA. We measured the significant difference in intensity across the recorded images, as the intensity had a larger signal-to-noise ratio, and this improved the implementation of the PIV algorithm. We then compared the PIV-estimated water depth with field measurement and observations, finding that the water depth was overestimated by 13.5%, which was primarily explained by non-linear wave breaking effects. We then introduced a correction factor, reducing the estimation error to within 6% of the true observed water depth.

Though there are limitations, this new approach can lower the cost of developing bathymetric maps in the nearshore and result in greater flexibility across space and time. Further improvements in equipment and work on developing better correction factors may result in still greater precision.

ACKNOWLEDGEMENTS

I would like to express my gratitude to my advisor, Dr. Kuang-An Chang for his guidance. Discussions and knowledge from our meetings have prompted me to further dig in the studies. Thanks to Dr. James Kaihatu who has been kind and takes good care of students. Working and chatting with him was an important and joyful experience pursuing my master's degree here in Texas A&M University. To Dr. Russell Feagin and Dr. Thomas Huff, I really enjoyed working with you, and you were always happy to share your knowledge. Also, I appreciate the assistance and the experience shared by Ms. Laura Byrd, Mr. Johnnie Reed, Mr. Kirk Martin, and my partner, Jin Young Kim.

Thanks to all my friends in College Station and friends from all around world. They have been supporting me technically and mentally. Since this paragraph is in the thesis, special thanks will be express to those who have given me related advice or have spent time with me on my defense practice, Dr. Chung-Kei Lai, Kevin Lin, Yu-Heng Lin, William Chen, Candice Chu, Shu-Hao Yeh, Yitsen Pan, Ting-Ju Chen, Yuan-Peng Yu.

Finally, my family has been very supporting just like those in happy movies or stories. I would go to them whenever I need to, and they would also be there for me. There are many more unlisted that I'd like to say thanks to, so in return, I hope I could be as supporting in the future to all my friends or colleagues.

CONTRIBUTORS AND FUNDING SOURCES

This work was supervised by a thesis committee consisting of Professor Kuang-An Chang, and Professor James Kaihatu of the Department of Civil Engineering, and Professor Russell Feagin of the Department of Ecosystem Science and Management.

This study is supported in part by the NOAA Texas Sea Grant College Program with a project titled “Study of wetland erosion due to storms through combined field, laboratory, and numerical investigations.”

TABLE OF CONTENTS

Page

LIST OF FIGURES

Page

LIST OF TABLES

Page

CHAPTER I

INTRODUCTION

This thesis introduces a method for measuring nearshore bathymetry using the unmanned aerial vehicles (UAVs) technology for data collection and the Particle Image Velocimetry (PIV) technique for video analysis. This method may lower the cost compared to traditional methods. Moreover, the mobility of the drone allows measurements to be done at different locations and at desired times.

Bathymetry has long been an important topic not only in geographical aspect, but also in coastal, environmental, and engineering fields. Especially, at neashore areas, the bottom topography is closely related to ship navigation, military usage [Williams 1947], sediment transport observation, oil drilling, other engineering constructions, etc. Moreover, water depth data provides important data for coastal simulation, which can be utilized for extensive purposes including but not limited to the applications mentioned above. For example, Elhakeem *et al.* [2007] included bathymetry in a model to simulate the oil spill in the Arabian Gulf region, which caused environmental pollution, and affected the industrial and drinking water. Maeda *et al.* [2011] combined the gauge data to run simulation and observed the development of a tsunami that hit Japan at the Tohoku coast line. Chen *et al.* [2006] further illustrated the principle for models using finite-volume method. Properties like current, tide, salinity can be successfully simulated. As the computational power improves, detailed phenomena may be explored with input boundaries (including updated and desired resolution bathymetry data) provided. While

information on bottom topography is extremely valuable, it is also difficult to obtain. As a result, there have been various methods proposed for deriving bottom topography.

The most straightforward type of survey technique is direct measurement. Traditionally, in situ survey using rod measurement was a labor intensive method with high risk. Then, tall tripod vehicle- Coastal Research Amphibious Buggy (CRAB) [Birkemeier and Mason 1984]- was designed to survey the nearshore area. With the development of technology, ships with measuring rope or sonar systems have proven to be a reliable method for collecting data as well. However, the sailing or operating time and location will be limited. moreover, the critical problems that make in situ measurement infeasible for some cases are the cost and sparse spatial resolution. In particular, this presents a problem for frequently changing nearshore bathymetry [Holman 1995], as costly data collection operations would be required to keep the results up to date.

Light detection and ranging (LiDAR) is one of the direct remote sensing methods utilizing the light penetration property to measure depth. LiDAR estimation leads to solid results with good spatial resolution [Irish and Lillycrop, 1999; Sallenger, 2003], and has been shown to be effective in experiments and in ideal water conditions. Unfortunately, it has not been able to perform quality measurement in all the oceans because many water bodies are covered with bubbles or are not clear enough for light penetration.

Alternatively, other kinds of remote sensing which can fix spatial resolution and time-consuming issues came into play. Unlike the techniques mentioned previously, most measurements using remote sensing are categorized as indirect methods. Instead of measuring the water depth directly, indirect methods basically work by recording surface

properties, such as wave speed, or wave frequency, and then fitting a model to relate the character with local water depth. Various approaches to collect data and different algorithms to calculate water depth are the two aspects that attract researchers to study, when applying indirect methods for bathymetry estimation. Satellite imaging and mounted cameras are possible tools to collect raw image data. In the 1970s, Polcyn and others conducted a series of studies about the application of passive remote sensing on measuring water depth [Polcyn *et al.* 1970; Polcyn and Lyzenga 1973]. The technique was mainly based on the ratio of radiance received in different spectral bands. However, ratio method is still being modified because the application is limited by the specific band needed. Also, survey was restricted to shallow water in order to receive sun glint from sea bottom. Stumpf *et al.* [2003] and Lyzenga *et al.* [2006] further utilized IKONOS multispectral satellite images to extract bathymetry in specified areas with different algorithms. Besides satellite imaging, other imagery tools and different types of data were also studied. Argus is a system with multiple cameras mounted on a tower to monitor coastal areas. It was introduced by the Coastal Imaging Lab in Oregon State University. At first, Argus was tested with different data collection and algorithm. After proven to have wide usage in many experiments, Argus stations have been reproduced at several locations [Holman and Stanley 2007]. Stockdon and Holman [2000] collected pixel intensity from one dimensional cross-shore array and applied the wave dispersion relation for estimation. Holman *et al.* [2013] further developed an algorithm, cBathy, to estimate two dimensional bathymetry mainly based on celerity. The Fourier transform was employed to analyze time series data in each pixel. Water depth best fit in the model was collected.

With the development of the UAV technology, there is potential in increasing flexibility of location. Moreover, repeated surveys can be performed without extra cost in equipment. From a coastal survey by Turner *et al.* [2016], the accuracy of present commercial drones was further illustrated. With RTK-GPS, no ground control point is needed for positioning, which means survey area can be expanded to the regions that are not easily accessed. In addition, the complex post-processing can be exempted. Dugan *et al.* [2013] employed the Fourier transform to the time series data acquired from an aircraft camera in order to retrieve the frequency-wave number spectrum. The results were combined with the dispersion relation to calculate water depth. In Splinter and Holman's [2009] study, instead of a time series video, only a single snapshot was needed to perform the algorithm based on refraction. However, this technique was limited by complex wave condition or small refraction conditions. In conclusion, previous studies show that remote sensing is a feasible tool to collect data with flexibility and lower cost.

Assuming the shallow water condition holds in the nearshore, the linear wave dispersion relation can be simplified to relate celerity and water depth. The relation implies that water depth can be derived from local wave speed. In the present study, PIV technique, which is a non-intrusive method suitable for analyzing image sequences is used to determine the wave speed. The whole-field velocity vector measurement without the need of physical measurement probes makes the PIV technique valuable in tracking fluid velocity. A book, Particle image velocimetry: a practical guide, by Raffel *et al.* [2013] illustrates the concept and principle of the technique. Also, many researches have been done employing PIV, ranging in geotechnical field for examining soil deformation [White

et al., 2001], wind tunnels to measure flow field near wind turbine blades [Ferreira *et al.,* 2009], and of course, diverse application in the liquid flow field, like eddies [Sheng *et al.,* 2000], microscopic scale flow [Meinhart *et al.,* 1999]. Besides its usages in different areas, extensions of the original techniques were developed. For example, tomographic particle image velocimetry (tomographic-PIV) is a technique that provides three-dimensional measurement [Elsinga *et al.,* 2006], and bubble image velocimetry (BIV) utilizes the intensity difference between air bubble and fluid as tracer instead of particle seeding. BIV can be applied in aerated region where no tracers can be detected if using PIV analysis [Ryu *et al.,* 2005].

Closely related to the present study, the traditional two-dimensional PIV have been applied to compute the velocity fields for a long time. Several applications focused on breaking waves in the surf zone [Chang and Liu, 1998; Cowen *et al.,* 2003]. In Melville and Matusov's [2002] research on breaking waves, PIV was employed to analyze aerial images taken downward at sea surface. With more than 30-year development and verification in diverse fields, the technique has a sound theoretical and practical basis.

In order to address the limitations of the existing methods, this thesis proposes an approach to estimating offshore bathymetry with drone video and the PIV technique. A quadcopter is easy to manipulate, and its ability to hover at a fixed location matches what is needed to record a set of time series data. PIV is a well-developed technique works to calculate the entire flow field. Taking advantage of the simplified approximation of the dispersion relation in shallow water, local water depth depends only on wave phase speed, which can be retrieved from aerial filming. Using this method, the updated bottom

topography near the coast line can be obtained after short calculation time, and can be done at almost anytime and anywhere the drone is allowed to fly. In addition, with the method proposed in the present research, a one-time cost of pursuing a drone covers all the cost needed for image acquisition. To sum up, the adjustable resolution, mobility, and relatively low cost show the value of this method.

Different kinds of equipment used to derive bathymetry data and application of the PIV technique have been introduced. Advantages of the method presenting have also been clarified in Chapter I. Background and basic knowledge about the wave dispersion relation and the PIV technique are required to hold the experiment. They will be introduced in Chapter II along with the specification and the field tests for the UAV used to conduct data collection. In Chapter III, step by step from experiment preparation and equipment, software setup will be illustrated. The algorithms used to retrieve celerity and estimate water depth will then be developed based on the data distribution. Two sets of experiment were performed at Freeport, Texas. The experiment condition and results including correction and discussion will be shown in Chapter IV. Summary will be made in Chapter V. Further improvement or extending application based on the proposed method will be discussed as well.

CHAPTER II

METHODOLOGY

2.1 Wave Theory

Laplace equation is treated as the governing differential equations to describe irrotational and incompressible fluid. Combined with boundary conditions like kinematic behaviors and dynamic properties at free surface and at bottom boundary, the linear solution represents the motion of gravity waves. Included in the solution, relation between wavenumber, wave frequency, and water depth is called dispersion relation:

$$\omega^2 = gk \tanh(kh) \tag{1}$$

where ω is angular frequency, g is gravitational constant, k is wavenumber, and h is water depth. In the shallow water condition, where kh is small enough ($kh < 10/\pi$), $\tanh(kh)$ approaches kh, and Eq.(1) can be approximated as:

$$c = \sqrt{gh} \tag{2}$$

where *c*, celerity, is determined solely by the water depth. In other words, if phase speed is known, water depth can be inversed. Eq. (3) can be rewritten for a clear explanation

$$h = c^2/g \tag{3}$$

which shows water depth is directly related to celerity, or we can say water depth is proportional to celerity square in shallow water.

Restrictions have to be considered in the present research as waves are assumed to be propagating in shallow water in order to satisfy the condition for simplified dispersion

relation. Small kh indicates small water depth or long wave length. Waves propagating under this condition are called long waves. Long waves may be tidal waves or swell created by severe weather event from far away. The wave lengths are long enough to reflect the influence of the bottom boundary condition, and they will not be affected by local wind a lot. These properties illustrate the rationale for applying Eq. (3).

When the bottom topography is not flat, the assumptions for the mild-slope equation have to be satisfied so that the waves will closely follow the Eq. (1) [Berkhoff, 1973, 1982].

$$O(\frac{\nabla h}{kh}) \ll 1 \tag{4}$$

Based on the restriction, the slope has to be small, and also the scale should be larger than the wave length to be reflected.

Non-linearity is another possible source that can lead to inaccuracy in this method, and should be explained with wave theory. Dispersion relation introduced above is a linear solution. However, it is non-linear wave that will be tracked in the present study. Moreover, when filming in the surf zone to include bubbles, the effect from wave breaking will also influence the results. Different kinds of models were built to estimate the non-linear effect. Svendsen and Hansen [1976] came up with one of the common forms to correct phase speed considering the effect of wave height (H) to water depth (h) ratio ($\frac{H}{h}$).

$$c = \sqrt{gh(1 + f(m)\frac{H}{h})} \tag{5}$$

Where $f(m)$ is a function depends on m, the modulus of the elliptic functions. Parameter m can be determined by wave number, wave height, and water depth. The frequency

dissipation effect is considered in Eq. (5). How to determine $f(m)$ then became an issue with different approaches. In the present case, the shallow water condition is assumed to be satisfied, and $f(m)$ will be close to 1. Eq. (5) can be rewritten as

$$c = \sqrt{gh(1 + \frac{H}{h})} \tag{6}$$

For breaking waves, similar models were developed. They may be more complicated with more than one form of water depth involved, such as, crest, trough, or mean level. To simplify, the shallow water approximation was presented.

$$c = a\sqrt{gh} \tag{7}$$

Constant a varies from different models. Schäffer *et al.* [1993] referred Stive's [1980] spilling breakers experiment and used 1.3 for a in Eq. (7). It was further examined again by Madsen *et al.* [1997] with Boussinesq model. The result shows that a=1.3 perform a close trend, but overestimated the celerity. From Stansby and Feng's [2005] laboratory measurement, a was between 1.06 and 1.32. Not only laboratory experiments were done, Thornton and Guza [1982] performed field measurements at a beach with sloping about 0.02. Local root mean square wave height to water depth, $H_{rms} \cong 0.42h$. Tracking in about 20 days, the measured mean celerity, which was collected from coherence peak of celerity spectra lies within 90% to 120% of celerity from the linear theory. That is to say, the constant a in Eq. (7) was 0.9 to 1.2 in their field measurement.

Catálan and Haller [2008] constructed a reduced scale bathymetry of field beach in a laboratory to collect wave properties with already known water depth. Data were retrieved from wave gauges and camera videos. Comparison were done between the

measured data with several non-linear models including the ones mentioned above. Errors were smaller when applying the models including correction with wave height. However, in the present application, we took advantage of the simplified dispersion relation, Eq. (2), to avoid the costly gauge measurements. Accordingly, models using only a constant, like Eq. (7), may be considered to correct the non-linear effect.

Inside surf zone, there still exist other reasons that make the depth inversion from linear dispersion relation inaccurate, such as reflection [Elgar and Guza 1985; Holland 2001]. Also, there are other models built to include the non-linear effect. For example, Grilli [1998] utilized the asymmetric wave shape to correct his depth inversion algorithm.

2.2 PIV Technique

Particle Image Velocimetry (PIV) is a well-developed technique to measure flow field. Taking advantage of its non-intrusive and whole field measurement property, PIV is a suitable method for the present case study.

Single-frame/ multi-exposure and multi-frame/ single-exposure are two common ways to collect image data and to track the seeding particles by the PIV algorithm subsequently. In the past when chemical, darkroom, and photographic paper were used for wet photography, single-frame/ multi-exposure was more popular than multi-frame/ single-exposure method because of the time required to analyze each frame. With the development of modern electronic image sensors, like charge-coupled device (CCD) and complementary metal-oxide-semiconductor (CMOS), digital cameras are widely used

nowadays. Digital PIV that utilizes digital camera to collect PIV image data was introduced. Each CCD pixel registered a different light intensity depending on the amount of photons that falls on it. After the charge are amplified and converted into voltage, the voltage will be digitized to integer numbers representing the light intensity. As a result, an image can be stored as a matrix containing digital numbers representing intensity information. With the development of computers, digital matrices can be stored and post-processed fast and easily. Accordingly, the convenient format makes digital camera popular when carrying out PIV research. In addition, the cost of multi-frame/ single-exposure method is now lower and thus the technique is widely used. For example, filming videos is a common data source for multi-frame/ single-exposure technique.

Typical application of PIV requires flow-tracking tracer seedings in the flow of interest. They are used as tracers to represent local flow field. Therefore, it is important to select the seeding or tracers that move inseparably with the fluid flow. To optimize the computation for accuracy, the density and the diameter of the tracers have to be chosen strategically. The selections of the properties are closely related to the estimated velocity, the time step between two exposures, and the interrogation window size, which will be discussed later. The general idea is to have enough tracers kept in the same interrogation window before and after the motions. Also, the seeding size has to be selected so that they are large enough to scatter sufficient light, meanwhile not too large to be able to follow the fluid flow perfectly [Keane and Adrian 1990; 1992]. In this project, air bubbles caused by wave breaking will lead to significant intensity difference from their surrounding non-

braking wave background in the images, and therefore they can be utilized as tracers instead.

To derive the velocity, we will first compute the displacement vector, $\vec{s}$, of tracers between two instances of time, or two consecutive video frames. The principle of double-frame/ single-exposure PIV will be illustrated with Figure 1.

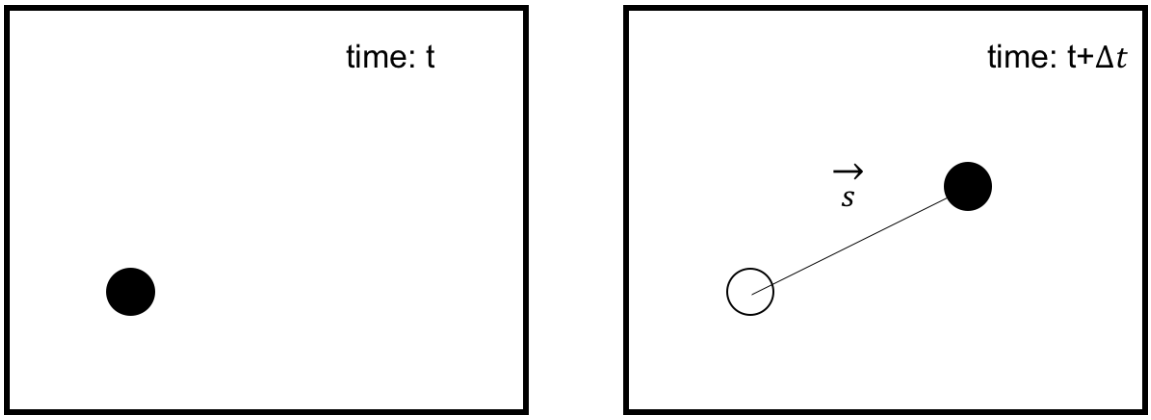

Figure 1. Double-frame/ single-exposure PIV. Black dots represent the particle positions at current time step.

Since Δt, the inter-frame time is known, the velocity vector, $\vec{v}$, can be derived using the equation

$$\vec{v} = \frac{\vec{s}}{\Delta t} \tag{8}$$

In practice, each image will be subdivided into an array of interrogation windows (also called subwindows), and the basic concept illustrated above will be applied to every window. After the velocities for all the windows are calculated separately, they will be combined to give the full velocity field of the entire image.

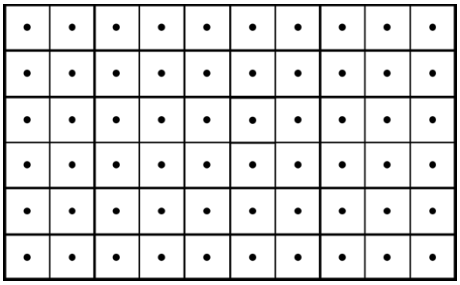

Figure 2. Image separated into interrogation windows. Displacement of each window will be presented at the center.

The cross correlation technique is applied to evaluate the displacements in every interrogation window between two consecutive frames. Cross correlation discrete function can be written as:

$$C(dx, dy) = \sum_{subwindow} I_1(x, y) I_2(x + dx, y + dy), -\frac{n}{2} < dx, dy < \frac{n}{2} \qquad (9)$$

Where C is a 2D correlation plane, I_1, I_2 are the matrices consisting of image intensities in interrogation windows of two images, x, y are positions, and dx, dy are displacements along x and y directions, $n \times n$ is the size of the interrogation window. For the calculation in the present study, dx, dy are set to be in the range $-\frac{n}{2} < dx, dy < \frac{n}{2}$, which means only displacements smaller than one half of the window size will be considered. This is also an important indicator when choosing a feasible window size, and will be further illustrated later in Section3.2. The pair of (dx, dy) that leads to the largest correlation value, $C(dx, dy)$, will be considered as the displacements of the interrogation window during the time Δt.

Since the (dx, dy) in Eq. (9) are integers, the calculated displacements in either x or y direction are integers. Consequently, maximum error can be up to ± 0.5 pixels. To

improve the situation, sub-pixel precision is introduced to recover sub-pixel accuracy via an interpolation around the found integer displacement peak in the correlation plane. In the present application, the three-point Gaussian function was used for curve fitting on the correlation value-displacement plot to derive displacement in each dimension.

One way to examine the settings and the results is to plot the velocity vectors with arrows and superimpose them on the original frames. The amplitude, direction, trend, and smoothness can be viewed and checked clearly. An example is presented in Figure 3. Similar method to examine the data will be used throughout the present study. However, in later figures, only a small part of the image may be shown in order to present the vectors clearly.

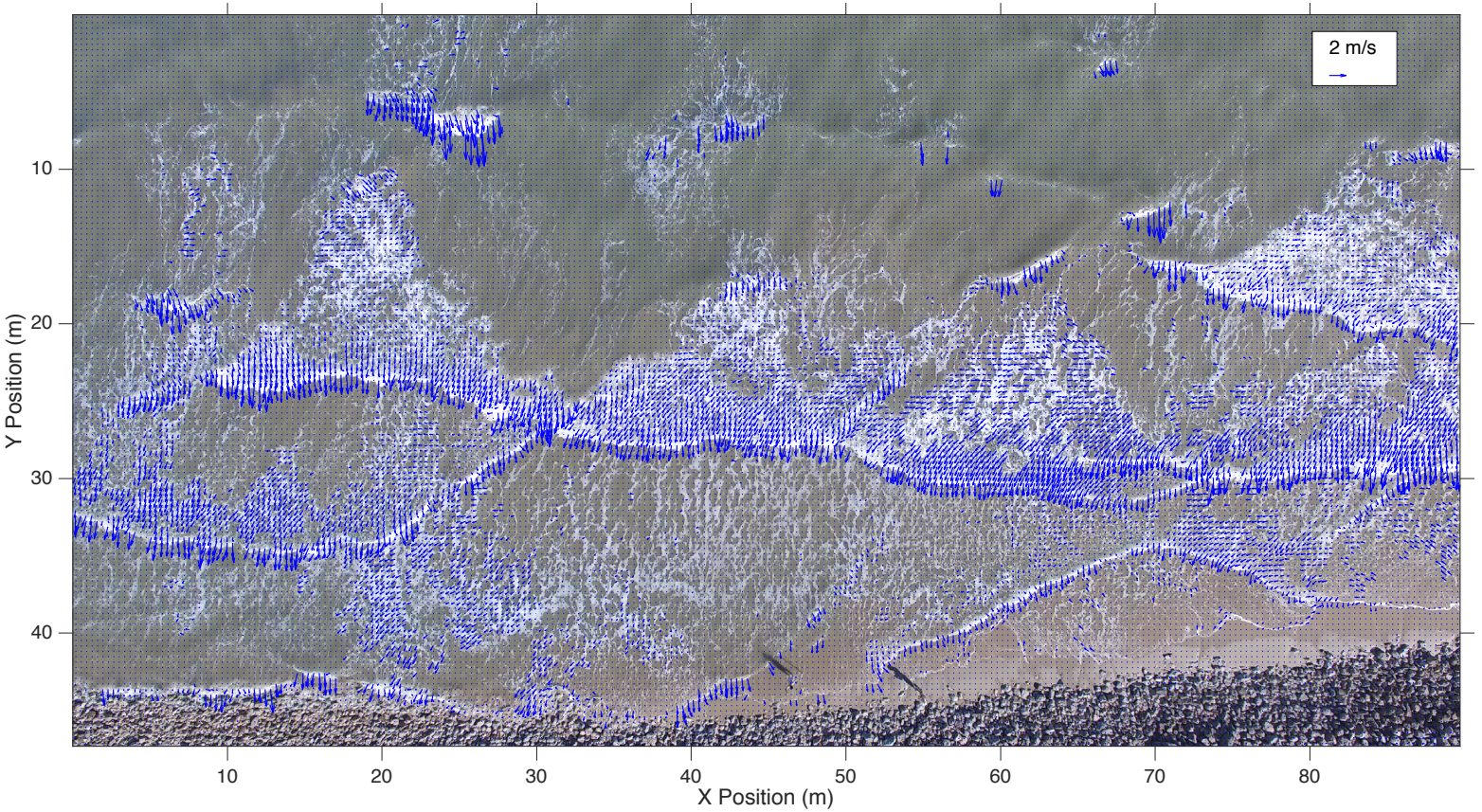

Figure 3. Calculated velocity vectors superimposed on image.

The source of error from a PIV computation can be categorized into outliers, the mean-bias error, and the root-mean-square (RMS) error. Outliers are the results from poorly matched particle image patterns, for instance, matching an out-of-window particle with a wrong one in the interrogation window. The resulting error is usually way off in both amplitude and orientation compared to its surrounding neighbors. As a result, they can be detected, and subsequently removed by its small cross correlation value, low peak ratio ($\frac{\text{highest correlation value}-\text{lowest correlation value}}{\text{second highest correlation value}-\text{lowest correlation value}}$), or by checking the vector distribution using images like Figure 3. Bias error is caused by bias correlation estimation. Mean-bias error is the difference between estimation and the mean displacement of the particles in the window; while RMS error is the root-mean-square of the differences between mean and the displacements of the particles. The magnitude of the errors can be quantified by comparing the PIV estimation with direct measurement or with image matrices generated numerically. Willert and Gharib [1991] analyzed images shifted by a known pixel distance relative to each other, and the RMS errors with different conditions were of the order of 0.1 pixel. Even with the lowest density (6 particles in a 32×32 pixel window) and the largest displacement (10 pixels), the RMS error was kept smaller than 0.16 pixel. Uncertainty has also been discussed a lot by others, like Westerweel [1993], Huang *et al.* [1997]. The mean-bias error, and the RMS error were measured under different displacements, and they maintain in the order of 0.1 pixel. Even though the RMS error became larger as the displacement increase, the percentage error actually decreased.

2.3 UAV Specification

2.3.1 Introduction

Considering both pricing and the specification, DJI Phantom 3 Professional was selected to be the UAV for this project. The Phantom 3 Professional is a quadcopter, a type of aircraft with rotors at four corners generating the propellers and provide the lift. Comparing to fixed-wing aircrafts, quadcopters can hover at an assigned location better, which meets the requirement of the designed experiment. This UAV comes with a camera and a gimbal system mounted on it. The Phantom 3 Professional is easy to control and is relatively stable when hovering. Still, operators have to be very careful especially when taking off and landing. Some key specs based on the manufacturer, DJI, website and my actual tests will be discussed.

The Phantom 3 Professional weighs 1280 g, diagonal size excluding the propellers is 35 cm. The remote controller can transmit up to 5000 m away; however, 120 m is the maximum height according to the US law. During the current experiments, horizontal distances from controller were set to be short, and heights range from 25 m to 120 m were attempted. When the aircraft hovers, the vertical accuracy is ± 0.1 m, the horizontal accuracy is ± 0.3 m with the Vision Positioning System; the vertical accuracy is ± 0.5 m, the horizontal accuracy is ± 1.5 m with the GPS Positioning System. Due to the height and the flying above liquid surface, the Vision Positioning System might not work properly in

the present study. GPS location and barometer height measurement will be displayed on the screen linked to the controller, and can be recorded and extracted with the image files. While the GPS and the Vision Positioning System help locating the drone, the built in IMU system collects linear and angular acceleration data which will be sent to the main processor to keep the aircraft stable during the flight. A battery provides the power to fly for more than 20 minutes after fully charged which takes about 80 minutes. The gimbal attaching the camera allows $-90°$ to $+30°$ tilt angle. In the experiments, it was always set to view vertically downward. Also, the gimbal provides buffers to reduce the drone tilting effect in order to stabilize the camera. The camera mounted can record videos with resolution up to 4096×2160 pixels, 8-bit dynamic range. With highest resolution, 24 frames per second (FPS) can be applied. The hovering stability and filming quality will be further examined as they are the most important aspects in the present experiments.

Since it is needed to determine the real object dimension from images, conversion coefficient was defined to relate the pixel size in images to dimension in real world. In the first trial to retrieve the scale, two water bottles were placed one meter away from each other as reference points.

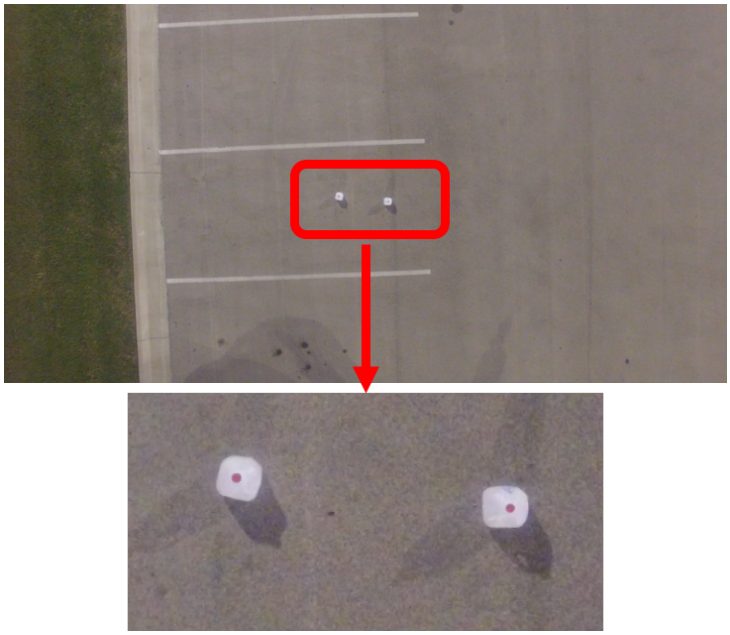

Figure 4. Two water bottles 1m away from each other were used as reference points to retrieve the centimeter/pixel conversion coefficients at different heights. Bottle centers were marked red for detection.

A video was taken with resolution 4096×2160, which was same as the one that will be applied to all the later experiments. After filming the bottles at different heights, frames were extracted from the video with MATLAB, and the pixel positions of the two bottles were detected. The pixel distance between those two bottle positions represented one meter in real world. As a result, the pixel-meter conversion coefficient was retrieved. Coefficients from pixel/meter were changed to centimeter/pixel which can make future conversion easier. When coefficients for multiple altitude were collected, interpolation can be applied to estimate the optimized height to fly at. Data with height from 5 m to 30 m are plotted below. Also it was noted that the result was close to a straight line because the angle of the lens was fixed, which led to linear relation between pixel distance and drone height. Compared with the linear fit, the standard error was 0.009. The highly related

result illustrated the accuracy of this test and the validation of height retrieved from drone data.

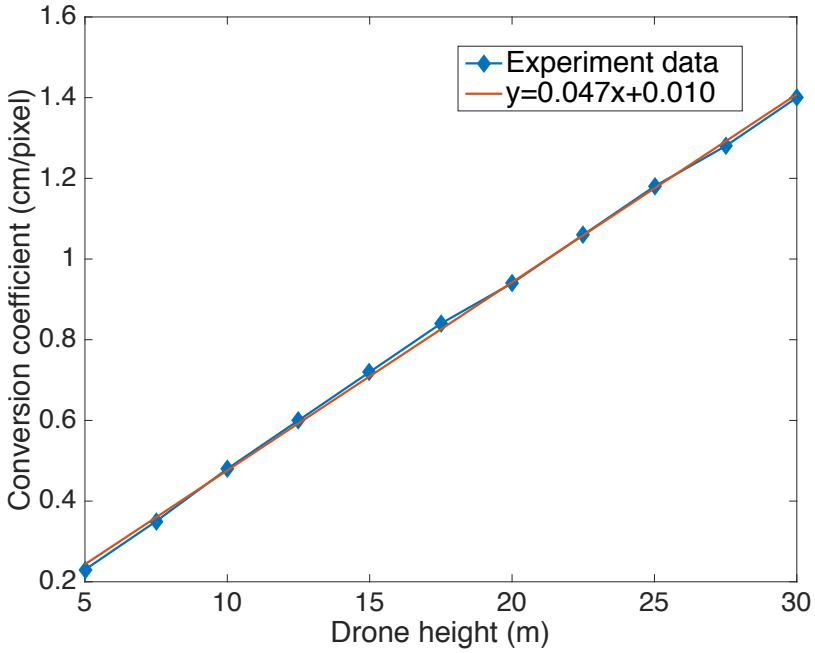

Figure 5. Pixel-to-cm conversion coefficient versus height. Data for drone hovering height from 5m to 30 m. Linear fit in orange line. Standard error: 0.009

This kind of data provided a key information to estimate the range to fly at. It was used during the preparation before flying at the area of interest. At this stage, the table did not have to be extremely precise because similar analysis can be performed again at the filming location or just simply include reference points in the video for conversion. During the final pixel-centimeter conversion coefficient test, the reference points were set to be farther away from each other in order do reduce the error proportion appear when detecting the reference points in the images.

2.3.2 UAV Test 1

As mentioned before, hovering stability was one of the most important drone property in the present study. Besides the official specification, some tests were done to examine how large the error could be if the drone was assumed to be hovering at a fixed location. Once again, filming resolution was set at 4096×2160 pixels, 24 FPS, drone flew at 20 m high, where 1 pixel in image spanned about 0.94 cm. Local wind speed was about 6 mph (miles per hour). One water bottle was filmed in the video, and the marked bottle center was to be detected. The main idea was that, the movement of the mark in the video was the opposite of the drone motion. For better detection, a colored frame was turned into a greyscale image, and the mean intensity of the whole image was subtracted in order to increase the signal-noise ratio. This technique will be applied again when preprocessing the frames for the PIV cross-correlation calculation. Two algorithms were used to detect the mark on the bottle. One was searching for the specific intensity representing the mark in the area which the bottle may move in and getting the pixel positions. The other was to use the PIV software directly to get the displacement of the bottle between frames. The results derived from the two methods agreed with each other. Only 30-second results from the first method, bottle detection, will be shown. In Figure 6, the displacements in two axes, dx and dy, compared with the original location is plotted. Obviously, we can see the effect of the wind. The bottle tended to move toward the negative x direction which indicates that the drone kept leaning to the positive x direction.

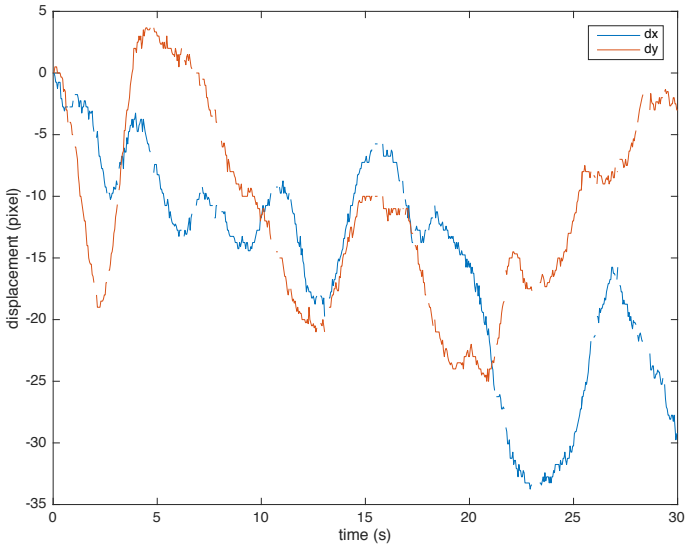

Figure 6. x-direction and y-direction position in time series

Recall that, the purpose was to quantify how much the hovering stability influenced the PIV results. Since PIV works between every two images, the bottle positions will be compared with their positions in the previous frames. The displacements in every time step are shown.

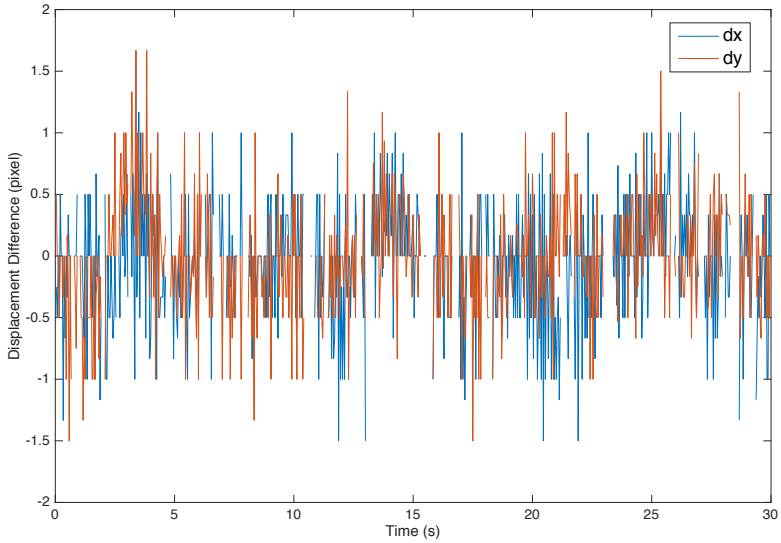

Figure 7. x-direction and y-direction displacements in every time step

Moreover, with equation $ds = \sqrt{dx^2 + dy^2}$, *ds*, the total error, which were the drone movements between frames were calculated and plotted. The root mean square error was 0.7 pixel in this test.

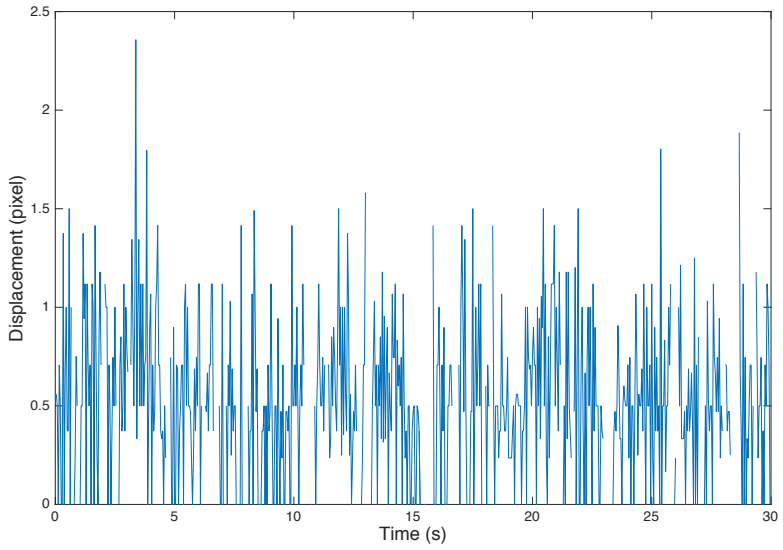

Figure 8. Total displacement in every time step

The similar process was carried out again during Experiment I, which will be explained later in Section4.1. The local wind speed was 17 mph, and drone height was about 50 m. The 30 seconds result root mean square error was 0.57 pixel. The drifting effect was smaller than the present case even though the wind was much stronger. One of the possible reasons was that, the instability at a lower level may be increased by turbulence near the ground. However, from my inference, the main reason may be the hovering height. When filming from farther away, the cm/pixel conversion coefficient was larger, which made the drifting error become relatively small in pixel.

Whether the error is acceptable depends case by case. Take the first filming error, 0.67 pixel, as an example, if the target object, which is wave, moves 6 pixels between frames, the error is about 11 percent; on the other hand, when the target moves only 2 pixels between frames, the error is can go up to 34 percent. Also, we observed that the

drone height and the local conditions can influence hovering stability greatly. If no further correction included, this kind of error should be considered.

2.3.3 UAV Test 2

The overall error caused by drone drifting has been quantified in the previous section. In this test, the influence of vertical hovering instability (heaving) on image scale will be examined. The UAV was set to hover at height between 50.4 to 50.8 m, which was about the filming height for one of the later projects (Experiment I); two reference points 22.1 m away from each other were targeted in the video. After a short filming, the drone was moved to a different height, and then it will be moved back to within the 50.4 to 50.8 m range to take another short shot. The steps were repeated several times. Since the angle of the camera lens was fixed, ideally, the reference points should always span the same amount of pixels in the images taken at the same height. After testing, the distance between reference points and the barometer height data were extracted. The averaged pixel distance was 954.6 pixels. The difference between data points and the mean were calculated as offset. The standard deviation of the offset was 2.8 pixels. It was divided by the mean, 954.6, and the result, 0.3%, represented the error caused by vertical hovering instability when a drone hovers within the 50.4 to 50.8 m range. Because the height, 50 m, was a pretty long distance, the results were very sensitive. Just a small vibration can lead to a visible change in the images. To sum up, if the variation is small enough, a few conclusions can be made. The barometer is reliable as the same heights measured turn to same pixel

distances. Also, if the vertically hovering variation during experiments is within a verified range, for instance 50.4 to 50.8 m, the error caused by this reason is acceptable (0.3%).

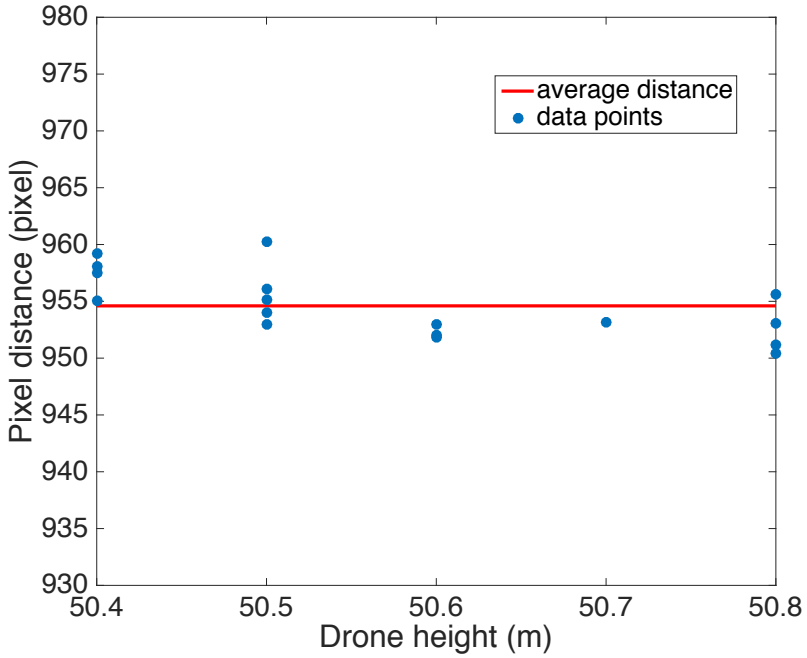

Figure 9. Pixel distance between two fixed reference points at height range within 50.4 to 50.8 m.

2.3.4 Camera Calibration

Due to the distortion effect of camera lens, the geometry of the targets may be changed in the images. Accordingly, when videos or images are applied in a research, it is important to perform camera calibration. The process of camera calibration is fitting the most possible camera parameters in the equation which describes how objects in 3 dimensional real worlds will be transform into the geometry we see in a frame. The results include camera intrinsic parameters which can be applied to back calculate the undistorted

images (calculated images assume no lens distortion). Besides getting better accuracy for the displacements calculated between frames, deriving undistorted images in the present research can also decrease the error when mapping the results back to the real world locations. The relationship between a 3D object and its projection in 2D image can be described by the function

$$sm = A[R\ t]M,\ \ A = \begin{bmatrix} \alpha & c & u_0 \\ 0 & \beta & v_0 \\ 0 & 0 & 1 \end{bmatrix} \tag{10}$$

where m is the 2D point coordinate; M is the 3D point coordinate, s is scale factor; $[R\ t]$ is the extrinsic matrix consisting of rotation and translation parameters which transfer M from world coordinate system to camera coordinate system; A is the camera intrinsic matrix with α, β represent the scale factors in two axes, (u_0, v_0) principal point, and c is skewness. More detailed information can be found in Zhang [1999].

In the present study, Zhang's method is used to retrieve the parameters including five radial and tangential distortion coefficients which allow users to estimate undistorted images. At least two images with a plane pattern at different orientations should be applied. Since the pattern, location and orientation are not constrained in any specific requirement, the equipment for this method can be easily prepared. Results will be derived by minimizing the equation,

$$\sum_{i=1}^{n}\sum_{j=1}^{m}\left\|m_{ij} - m(A, k, R_i, t_i, M_j)\right\|^2 \tag{11}$$

m_{ij} is the point position in the image, and $m(A, k, R_i, t_i, M_j)$ is the position calculated with Eq. (10) and k being coefficients of radial distortion.

The calibration in the present research was carried out with Camera Calibration Toolbox for MATLAB. Due to Bouguet [2000], at least two images should be utilized to process this calibration method. However, Zhang [1999] suggests that error will be decreased when more images are applied. The relative error becomes small as more than 15 images are used for calculation. 22 images with a planar checkerboard pattern located at different positions and different orientations were used in the calibration here.

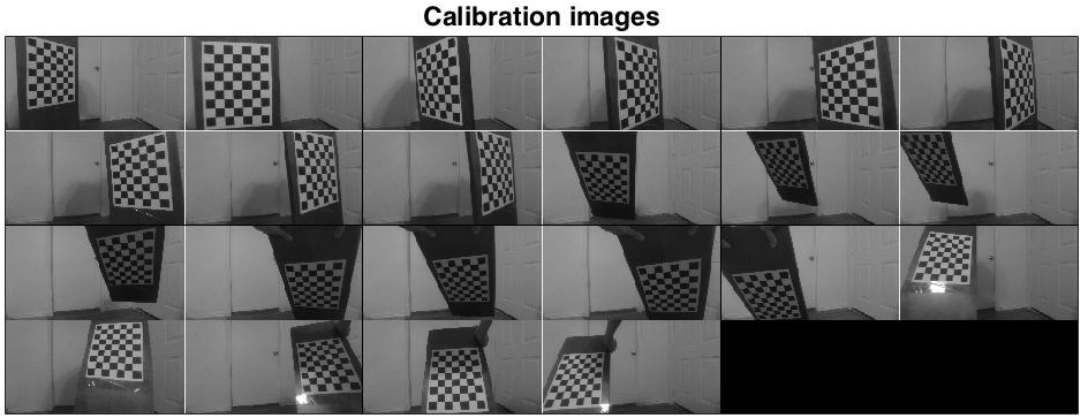

Figure 10. Calibration images. 22 images each with a checkerboard at different orientation.

After selecting the corner points for the MATLAB program, the orientation in each image and the camera parameters were calculated.

Table 1. Camera Calibration results.

Camera Calibration	
Focal Length (pixel)	[2310.77542 2299.86535]
Principal Point (pixel)	[2038.36223 1077.31329]
Distortion Coefficients	[-0.13033 0.09146 -0.00050 -0.00220 0.00000]
Pixel Error (pixel)	[0.93250 0.81314]

In distortion coefficients matrix, radial distortion coefficients (1st, 2nd, and 5th element) and tangential distortion coefficients (3rd and 4th) were included. They can be applied to calculate the undistorted images. One set of original and undistorted image pair are shown in Figure 11 as an example. The red lines are fitted to connect two corner points as auxiliary. In the original picture, the gap between the red line and the pattern is obvious; however, this phenomenon is fixed in the undistorted one.

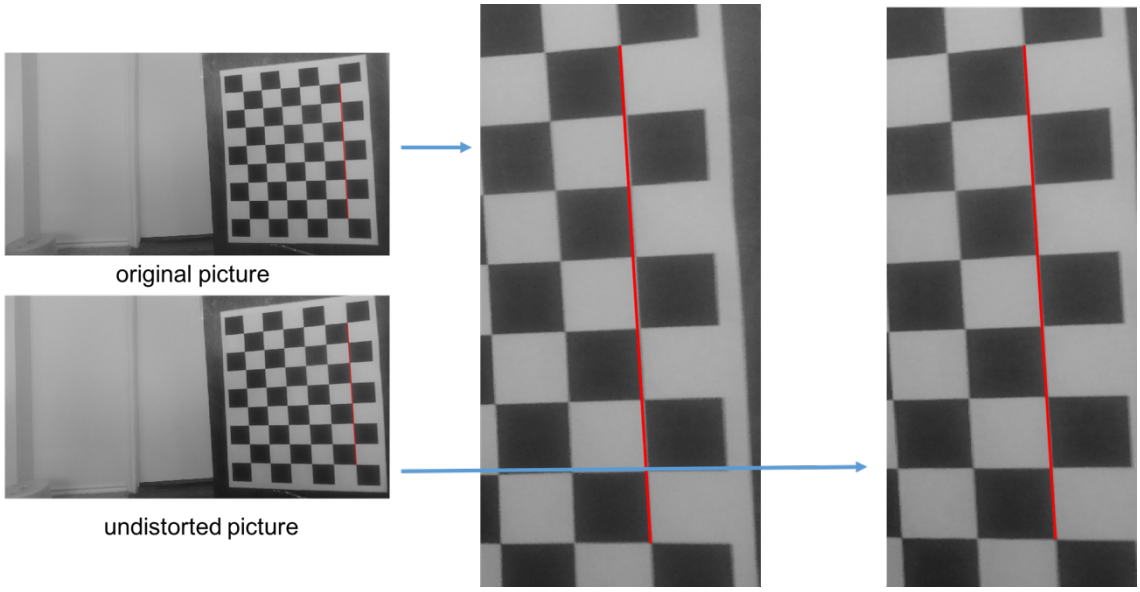

Figure 11. Calibration results. Original image compared with an undistorted image. Red lines connecting two points are used as auxiliaries to see the difference.

CHAPTER III

EXPERIMENT SETUP AND ALGORITHM

3.1 Introduction

To begin this chapter, the whole experiment process will be organized and briefly illustrated. The Phantom 3 hovered stably above the area of interest for a period of time to take a video with camera facing vertically downward. If the circumstances allow, fixed reference points would be included in the video for pixel-meter converting and removing drone fluctuation effect (will be performed in Experiment I, Section4.1). After the filming, the video was separated into frames and undistorted using the matrix derived from the camera calibration.

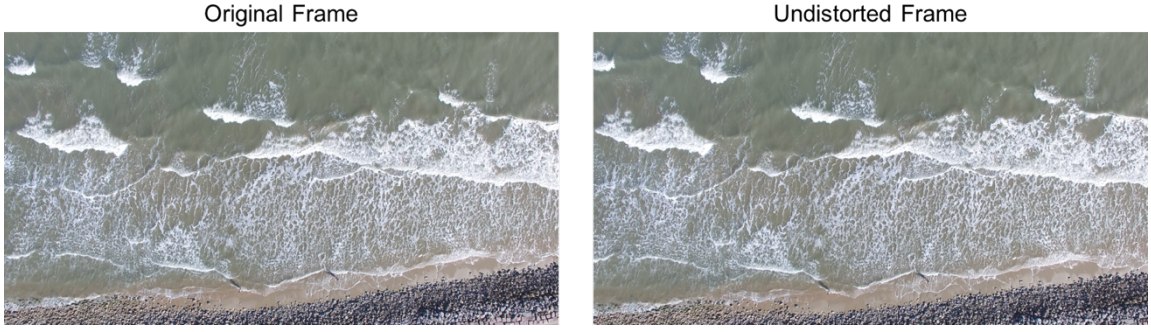

Figure 12. Comparison of original and undistorted image from a field video. The riprap area at the lower right corner shows significant distortion clearly.

The undistorted images were then processed with PIV analysis. In the present study, commercial software, DaVis, was applied. The images were divided into several interrogation windows depending on the selected window size, as illustrated in Section2.2.

The output from DaVis were the velocity vectors at all the grid points. Grid resolution were formed according to the selected window size and the overlap between windows (Section3.3). All the data were collected and several algorithms were designed trying to perform the best filtering and extracting the possible long wave phase speeds. With the wave speeds at nearshore area, dispersion relation in the shallow water condition, Eq. (2), was applied to calculate the water depth at each grid point. After calculating the water depth for enough points, we were able to construct the bathymetry. Furthermore, a smoothing was done to better fit the real topography.

3.2 Surveying Condition

If we have a rough idea what the wave speed (or water depth) might be, it can provide us with a clue of how high to fly at. For example, if the water depth is assumed to be 1 m, from Eq. (2) the celerity is about 3.2 m/s. While the frame rate of the camera is set at 24 FPS, the displacement between frames is about 0.13 m, which is 13 cm. Another aspect is about the PIV setting. The PIV technique calculates more accurately when displacement is smaller than one fourth of the interrogation window size. Also, it only works when displacement is smaller than half of the window size. Moreover, from experience in previous work referred in Section2.2, 32×32 window size provided solid performance and were typically used. If the interrogation window is set to be 32×32, displacements smaller than 8 pixels along either direction will be anticipated to lead to a satisfying result. On the other hand, the PIV algorithm error is of the order of 0.1 pixels

(Section2.2), and the percentage error will decrease as displacements increase. Aiming to make the PIV error ignorable, the displacement is better to be as large as possible in this case. As a result, 8-pixel displacement might be the optimized assumption.

Combining the 8-pixel assumption with the 13 cm displacement from the estimated wave speed mentioned above, the cm-pixel conversion coefficient can be derived. According to data like Figure 5, we can aim for a coefficient about 1.6 cm/pixel (13/8), and the optimized hovering height can be revealed. The method introduced is a way to get a sense of the optimal height for filming. However, we need to consider various trade-offs when determining the filming height. For instance, when the camera can not capture the texture difference clearly, maybe users should fly closer to the sea surface. On the contrary, if larger area must be included, users may want to fly higher. From my own experience, some part of the determination is a process of compromising. With so many uncertainties, like wave speed, interrogation window size, resolution, filming height, etc., trial and error can also be a way to help get a reasonable height. Also, trial and error may be the only way to determine drone height when we have no clue.

As mentioned before, instantly collecting data at any time is one of the greatest advantages of this new method to estimate nearshore bathymetry, but there are actually some conditions that provide a higher chance to extract accurate results. Weather conditions is one of the key factors which will be discussed here. Besides harsh weather events, like rain or hurricanes, that do not allow UAVs to take off, there are some other criteria that influence the experiment schedule. Early mornings or evenings are possible time periods for filming in order to avoid sun glittering. When the angle of sunlight is not

small enough, the reflection may be recorded in the video. Covered by shiny white light, no data in the affected region can be used. Some tests about sun glittering were done by Mount [2005], but the sunlight condition also depends on latitude and time in the year. On the other hand, a cloudy day can be another solution to prevent this phenomenon.

Since long waves are the waves showing the restraint from boundary conditions and following dispersion relation, long waves are the only targets in the present study. Consequently, the ideal condition may be calm local weather that does not create complex swells, but a severe weather event at the other side of the ocean which occurred a few days ago. It can create the long waves and might assist the waves to propagate completely.

During the present study, a test at a lake and one at a bay area were performed. However, the results were not smooth so they were not reasonable. No long waves to reflect the bottom boundary condition (water depth) was inferred to have caused the failure. Surfside Beach, Texas was then selected as the measurement area since long waves can be expected at the open beach facing the Gulf of Mexico.

3.3 PIV Setup

DaVis software by LaVision was the program applied to do PIV analysis in the present study. DaVis is a commercial software with multiple types of processing and parameter adjustments included. If this is not accessible, MATLAB open source MPIV [Mori and Chang, 2003] can be an alternative well-developed program for running PIV. DaVis offers advanced techniques from pre-processing to post-processing. For the

analysis in the present projects, only the basic image pre-processing and the PIV computation were applied. After importing the frames, subtract sliding background was selected as image pre-processing. Subtracting sliding background provided a constant background, which raised the signal-noise ratio especially in the blur areas. To be clear, two terms related to background intensity and contribute to correlation peak value were eliminated. They were the values caused by mean intensity correlates with itself, and with fluctuating intensities [Westerweel 1997]. By eliminating the two terms and increasing the signal-noise ratio, subtracting the mean image intensity led to easier and more accurate calculation. In addition, comparisons were done before applying image pre-processing to future works.

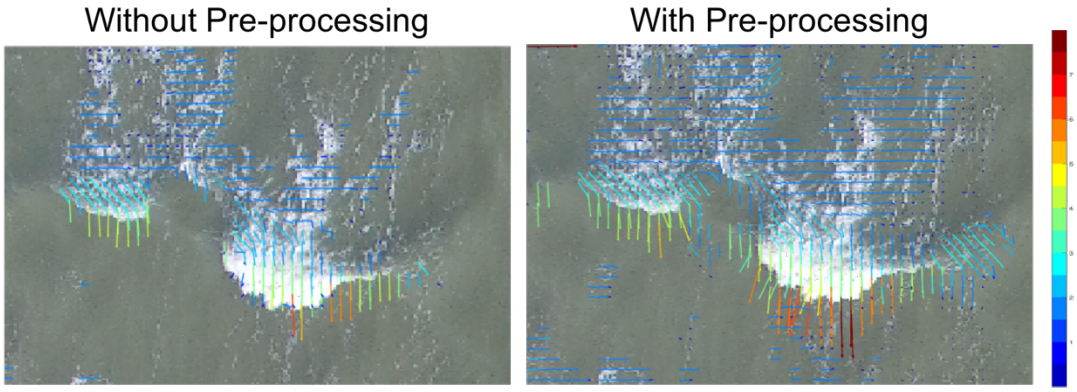

Figure 13. Comparison of results with and without image pre-processing. Arrows were color based on displacement magnitude. Only a selected area is presented.

The simplest way for me to examine the DaVis output data file was to use quiver command in MATLAB to plot arrows representing the calculated velocity vectors, and superimpose the arrows on the undistorted frames, as shown in Figure 3. From Figure 13, the results with and without image pre-processing actually seem to be very similar. However, the pre-

processed image leads to more wave front displacements calculated, while the original image may include more stray vectors.

About the settings for PIV, cross correlation was the chosen calculation mode as illustrated in Section2.2. Each interrogation window was set to have 50% overlap with every window right next to it. For example, a 32×32 square window covered the 9st to the 40th pixel in x direction. With 50% overlap, the window next to it spanned from the 25th to the 56th pixel along x axis. From the 25th to the 40th pixel, there were 16 pixels, which was half of 32 pixels, overlapped.

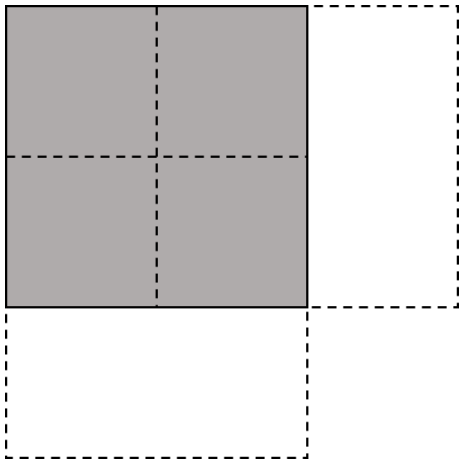

Figure 14. Fifty percent overlap. Grey square showing an interrogation window with dash line showing the neighboring windows at the right and below.

When choosing the interrogation window size, 32×32 was the priority. In some of the present cases, 64×64, 16×16 or even 8×8 were also tested. The velocity vector calculated represents a concept of averaging [Westerweel 2008]. All parts in the window may contribute to the highest cross correlation result. In most PIV cases, the local velocity is anticipated. In other words, the velocity gradient should be presented, which means

window size can not be too big. On the other hand, the whole wave front should be covered in the same window in the present research, and the error from PIV should be considered as well. The solution which satisfied these two aspects was a larger window size. In conclusion, choosing what window size to apply was again a process of compromising. Looking into the results of a few random frames may help making the decision. It was noted that the camera was set at 24 FPS. If the results show that the displacements are too small, users can also try import only one every two frames, which works the same as filming with 12 FPS. Consequently, larger displacements can be expected.

3.4 Algorithm

After calculation, data were then outputted and examined to develop a suitable post-processing algorithm for each individual case. In all the present projects, the output extracted from DaVis was the displacement vector (Setting time step 1 in DaVis; multiply by FPS to convert to velocity vector) at every grid point. MATLAB was used to read the data file, and put x direction displacement, u, and y direction displacement, v, into matrices. In addition, arrows representing displacement direction and magnitude were created and superimposed on the video frames as shown in Figure 3. From the calculated displacement field, post-processing algorithm were developed starting with filtering.

First, the undistorted colored images were transferred into black and white images with a reasonable user defined intensity threshold. In addition, dilation of the white region was performed in order to keep the data near the original black and white edge. Threshold

and dilation size were determined by testing a few frames. Since the video was filmed at a fixed location during a short time period, the intensities in all the frames were similar. Consequently, it was reasonable to apply the parameter decided with only a few frames to to every image. The binary image matrices were then resized to the same size as the PIV data matrices.

Figure 15. Binary image used for filtering. Data at the black region will be considered as bad data and be deleted.

Superimposing the binary matrix on the displacement matrices formed a preliminary filter to eliminate the data that were not in the desired region. The zeroes in the binary matrix indicated the black regions, which were the locations with no breaking waves. It was noted that the binary image matrix was used only for preliminary filtering. It was the color image that the researcher imported to DaVIS (Section3.3), and it was converted to gray scale for PIV computation.

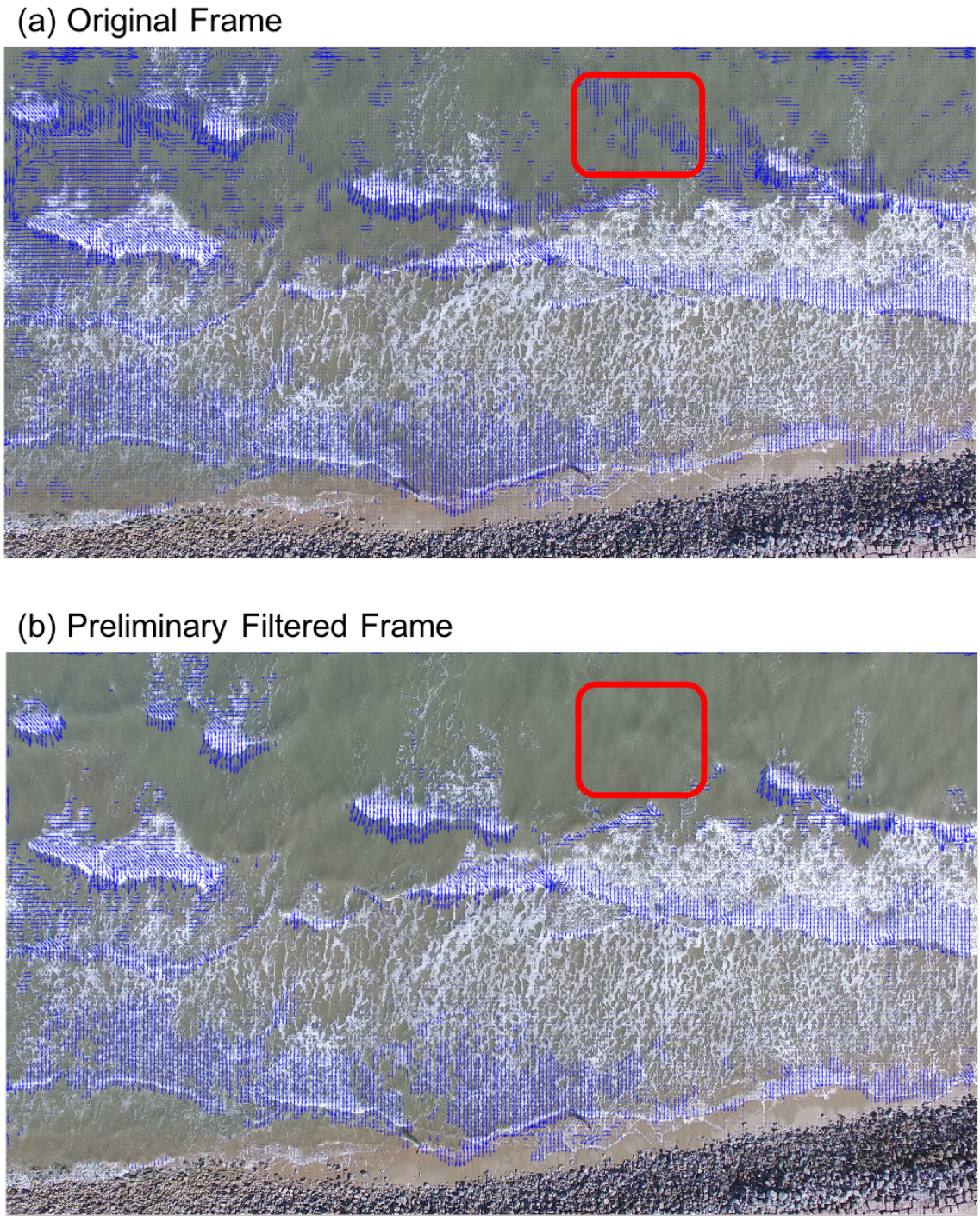

Figure 16. Comparison of results before and after preliminary filtered. Focus on the areas like the red box, vectors in the region with no breaking wave passing through were eliminated.

Figure 16 is a comparison showing the filtered results. Data in regions like the red box are being eliminated out.

After studying the matrices, images, and video, it was observed that maximum displacements always appeared at the wave front, following were a few decreasing displacements, and then tiny displacements separated in the other parts in surf zone and swash zone.

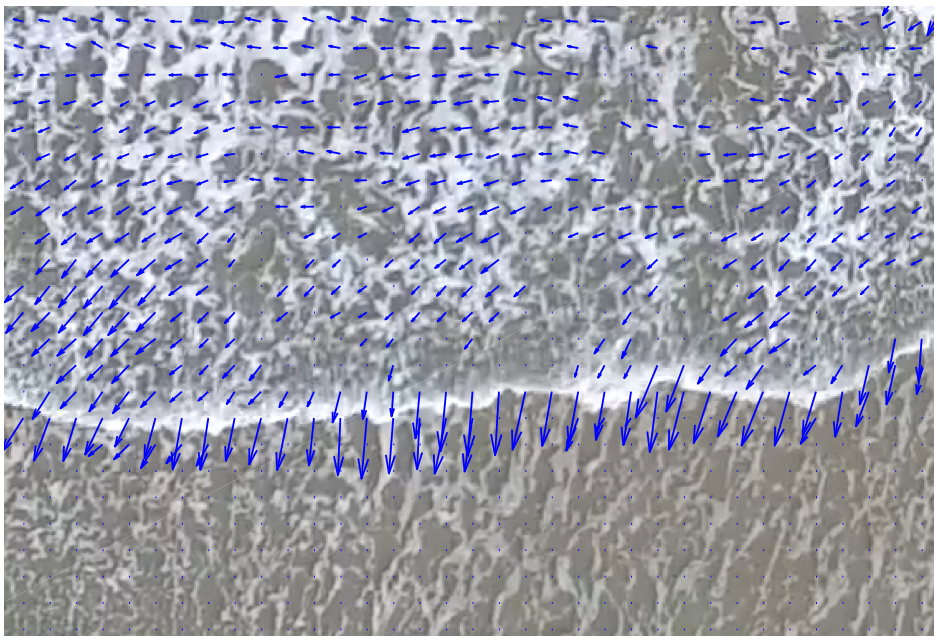

Figure 17. Displacement distribution. Image frame with vectors superimposed on it was used for examination.

The particle speeds at where the wave just broke were closest to the celerity. Combining these observations, the local maxima in the white bubble region were defined as the good vectors, which may represent long wave phase speeds. To make the data selection easier, the videos were taken with image y axis parallel to the wave propagation direction, which is usually close to cross-shore direction. In this situation, every displacement matrix was

separated into single columns. The local maxima in each column essentially represented all the local maxima in the images since none of them overlapped one another when the waves propagated along y. In my algorithm, absolute threshold and relative threshold for selecting the local maximums were defined by checking the displacement data in sufficient amount of column vectors. In Fgure.18, spatial domain data in a random column is shown.

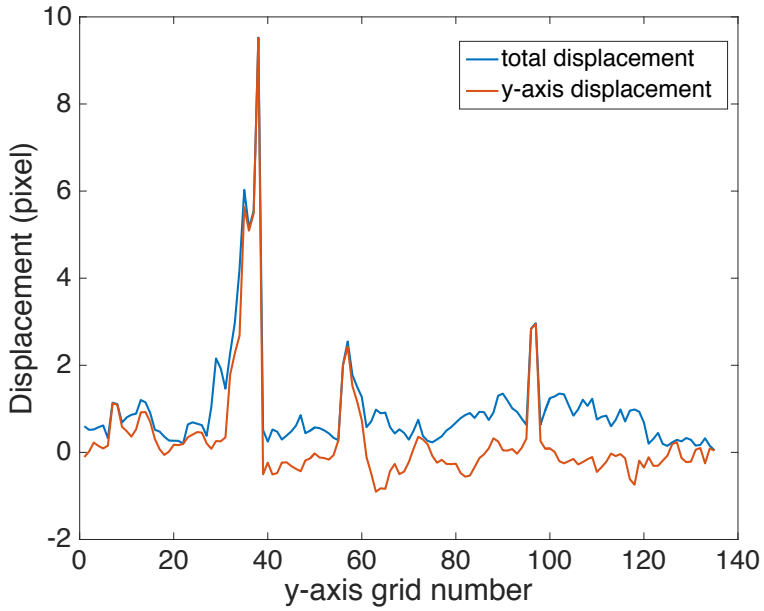

Figure 18. y-direction displacement and total displacement data in a random spatial domain column. Wave front displacements are the local maximums.

The magnitude of total displacement and y-direction displacement were plotted against y-axis grid number. Positive y direction was the on-shore direction. As one can observe from the plot, the signal-noise ratio was high. Accordingly, the threshold setting did not have to be very strict in this case. In addition, Figure 18 also shows that the y-direction displacements dominate the total displacements as the y-direction displacement curve is

pretty close to the total displacement curve. Correspondingly, the distribution proved the validity of the method making the camera view parallel to the wave propagation direction.

Moreover, the range where the good u, v vectors fell in were also examined. The highest and the lowest threshold for u and v were set in order to remove some stray vectors caused by fail calculation or noise in the videos. When one of u or v was not in the acceptable range, that vector would be eliminated. Except for the good data, the rest positions were replaced by NaN flags in the MATLAB displacement matrices. With distribution in the cases, this algorithm worked well as illustrated in Figure 19.

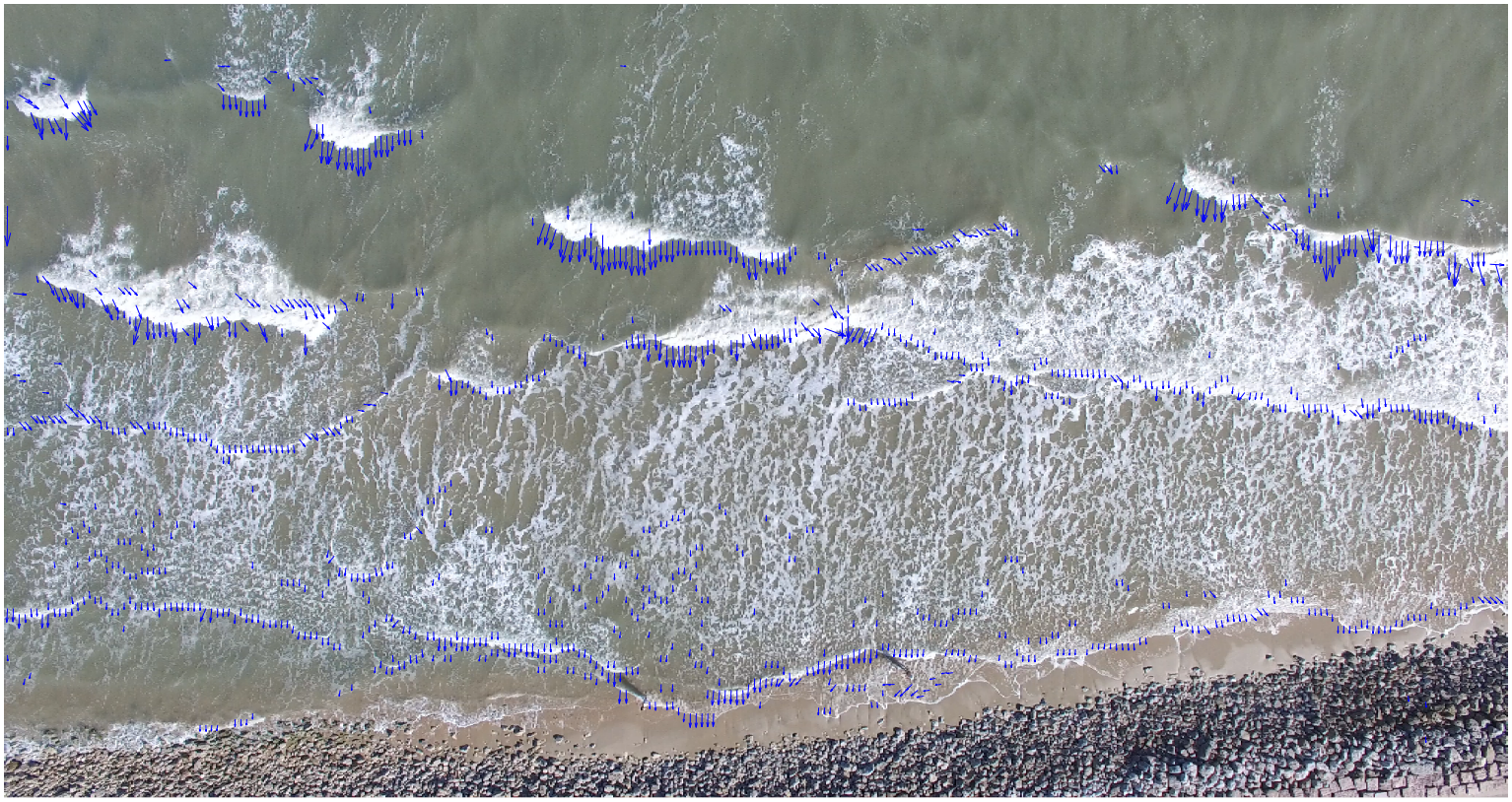

Figure 19. Displacement vectors in a frame after filtering. The remaining vectors were considered as good data and stored in the displacement matrix.

After examining the results from a few frames, all the thresholds were determined. Since the video was filmed at a fixed location, the valid celerity at the neighborhood grid points should be very similar in each frame based on the similar water depths. Accordingly, the criteria decided above was applied to all the frames from the same video. With the parameters set, a user defined MATLAB program was run to process all the frames and data to go through the algorithm and collect the good data. Filtered displacement data were stored in a three dimensional matrix, where x direction represented the x axis grid number, y direction represented the y axis grid number, and z direction represented the frame number. As one may expect, most elements in the matrix were NaN because wave fronts only appeared in a few interrogation windows in each frame.

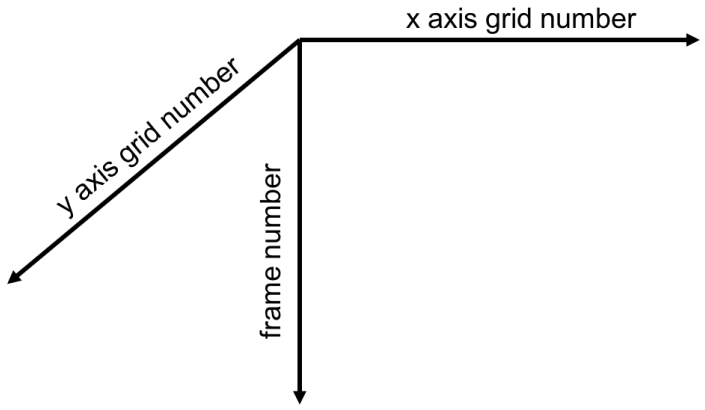

Figure 20. Three dimensional displacement matrix storing displacements with x direction represents x axis grid number, y direction represents y axis grid number, and z direction represents frame number

For every fixed x, y position in the matrix, all the z showed the valid wave front displacements as a time series data. All types of waves and events may be included in the

current data. Theoretically, only the largest displacement represents the local celerity. However, due to the errors in all the process and the uncertainties in environments, different algorithms were attempted to derive a suitable data collection.

Before introducing the next step of the post-processing algorithms, more about the data set will be examined. If the results are as expected, it is reasonable to conclude that the calculation and all the settings are feasible. The flow field was checked by images with velocity vectors, like presented in Figure 3. Images like this were further edited to rebuild a short movie showing the calculated vectors superimposed on movie with propagating waves. Since the fluid motion is always continuous, it can be observed in the video if something goes wrong.

Besides checking the imagery, data were also examined. Starting with the three dimensional matrix described above, a fixed x and fixed y grid point (better to be close to reference points with known water depth if applicable) was chosen to check the time series data showing the valid phase speed when wave fronts propagated through the chosen window. The data from the first set of experiment, Experiment I, which will be present in the next section, was used as an example. To briefly introduce the background, Experiment I was done at Freeport, TX. Two individuals were standing in the water with stick measurements to measure local water depth. They were filmed in the video in order to identify the measurement location. A short part of the time series data at a random fixed location is shown in Table 2.

Table 2. Typical data type of a selected grid point. Calculated displacement data of first 1136 points are shown. NaN flags in between are omitted.

Frame Number	...	102	103	104	105	106	107	…	211	212
Displacement (pixel)	…	NaN	1.49	2.10	2.16	2.74	NaN	…	NaN	1.20

213	214	215	216	217	218	219	220	221	…	664	665	666	667
1.75	0.95	1.66	1.66	1.86	NaN	2.27	1.62	NaN	…	NaN	4.82	5.29	5.40

668	669	670	…	675	676	677	678	679	…	1128	1129	1130	1131
4.00	4.58	NaN	…	NaN	2.85	2.48	3.62	NaN	…	NaN	2.35	2.88	3.75

1132	1133	1134	1135	1136	…
3.82	3.13	3.29	2.88	NaN	…

In the table, the NaN flags between valid displacements were omitted. Groups of continuous valid data appeared when a wave front traveled inside the interrogation window. In 1136 frames, which was about 47 seconds, five waves passed by and were detected (the 212nd to the 220th frame were inferred to be caused by the same wave). Whether the average or maximum displacement of each group can represent the displacement of the wave will be discussed later. For now, it is reasonable to apply the mean concept. The average of the five groups were 2.13, 1.62, 4.82, 2.99, and 3.16 respectively. Between these data, 4.82 displacement may be closest to the actual celerity since it was the largest one. This was a typical type of data. Most of the grid points showed the same type of data but with different displacement magnitudes. Now, a comparison between two fixed locations near each other will be done. To make the table clear, only the valid data and their frame number will be presented. 32×32 window size was used in the calculation.

Table 3. Valid time series data at two selected points. (a) 1st Set (119, 39) (b) 2nd Set (120, 35)

(a) 1st Set Grid Number: (119, 39)

Frame Number	225	226	227	678	679	680	1263	1264	1353	1354
Displacement (pixel)	3.80	4.69	4.22	6.71	4.70	5.96	2.52	2.13	2.74	2.44

1355	1434	1435	1436	1638	1639	1640	1641
2.66	3.49	4.47	3.75	2.50	2.83	3.68	3.27

(b) 2nd Set Grid Number: (120, 35)

Frame Number	97	98	99	215	216	217	384	385	668	669
Displacement (pixel)	1.80	1.73	1.87	3.64	3.68	3.89	2.88	3.00	4.59	5.06

675	676	1246	1247	1248	1249	1250	1251	1422	1423	1625	1626	1627
1.93	2.45	1.61	1.99	3.01	1.62	2.57	2.00	4.44	3.51	4.03	4.19	4.54

Some groups in the two sets of data were marked with the same color because they were hypothesized to be induced by identical waves. This hypothesis was established due to the displacement magnitudes and the frame number where the wave fronts occur. As a reminder, the video was taken with waves propagating toward the positive y direction. Since y was at the 39th grid point for the first location while 35th for the second set, this indicated the first location is about 64 pixels ($\frac{32}{2}\times(39-35)$) away from the second location in the y direction. While the first set was at the lower part of the image where waves traveled toward, there was a lag in the frame numbers for the same wave in two sets of data. In other words, waves first traveled through the 2nd point, and then appeared in the 1st location later. The lags for different events were similar when the phase speeds were similar. The data type was like the case listed in Table 2, and the relation between

the data of the two locations compared here can be reasonably explained. In other words, the settings and the algorithm until now make sense.

Basic principle for choosing window size have been illustrated before. Here, a comparison between 32×32 and 64×64 window sizes will be compared. Data was also gathered from Experiment I. The fixed x, y, which is the same as the first location in Table 4 (1st Set, Grid Number: (119, 39)), was again selected to collect the time series data. Using the same indication, the groups inferred to be induced by identical waves were marked with the same color. In this case, the frame number and the displacement magnitude showed similar results even with different window sizes. Due to larger window size, the time each wave front appeared in the 64×64 interrogation window was about twice of that in a 32×32 window. Another phenomenon was that the larger window size captured more wave events in this case. This may happen because of the local wave breaking pattern. From the comparison, the results from different window sizes were consistent. Considering the resolution and the velocity gradient, smaller window size, 32×32, was applied. However, if the extra events in 64×64 results were determined to be the desired phase speed, larger window size could have been chosen to increase the sample amount, which may lead to a more accurate result.

Table 4. Valid time series data at same grid points calculated with different interrogation window size. (a) Window Size: 32×32 (b) Window Size: 64×64

(a) 1st Set Window Size: 32×32

Frame Number	225	226	227	678	679	680	1263	1264	1353
Displacement (pixel)	3.80	4.69	4.22	6.71	4.70	5.96	2.52	2.13	2.74

1354	1355	1434	1435	1436	1638	1639	1640	1641
2.44	2.66	3.49	4.47	3.75	2.50	2.83	3.68	3.27

(b) 2nd Set Window Size: 64×64

Frame Number	109	110	111	112	113	114	224	225	226
Displacement (pixel)	1.41	NaN	1.87	1.56	2.42	1.28	4.13	4.01	4.43

227	228	229	395	396	397	398	399	400	401	676	677	678
4.45	4.59	4.65	5.91	5.09	5.69	4.89	6.20	5.51	5.21	5.73	5.63	7.44

679	680	681	682	1142	1143	1144	1145	1146	1262	1263	1264
4.98	4.50	5.56	6.36	3.79	4.34	4.09	2.62	3.69	1.75	2.21	1.92

1353	1354	1355	1356	1357	1358	1359	1431	1432	1433	1434	1435
2.40	2.04	2.39	2.61	3.52	2.98	2.91	4.26	4.91	4.63	3.49	4.35

1436	1637	1638	1639	1640	1641
3.91	4.62	4.45	4.69	4.92	4.74

After checking the validity of the method and examining the data, the algorithm for long wave phase speed extraction will now be discussed. We will refer to the two algorithms as Algorithm I and Algorithm II. To begin, the average displacement of each group mentioned in the previous paragraph was calculated as the displacement caused by the wave. With each single wave speed determined, Algorithm I picked the highest portion, which may be the top one third or the top one fourth or other user defined fractions, and the algorithm was designed to find the average of the group. If the standard deviation of

the collected data was larger than a user defined threshold, one data point would be eliminated. The selection process was to compare the standard deviation without the largest and the smallest data. The one which led to the larger standard deviation would be canceled. This process kept working till the standard deviation was smaller than the user defined threshold, or when there were only two data left. The highest speed was not selected solely in order to avoid results from bad calculation or video noise.

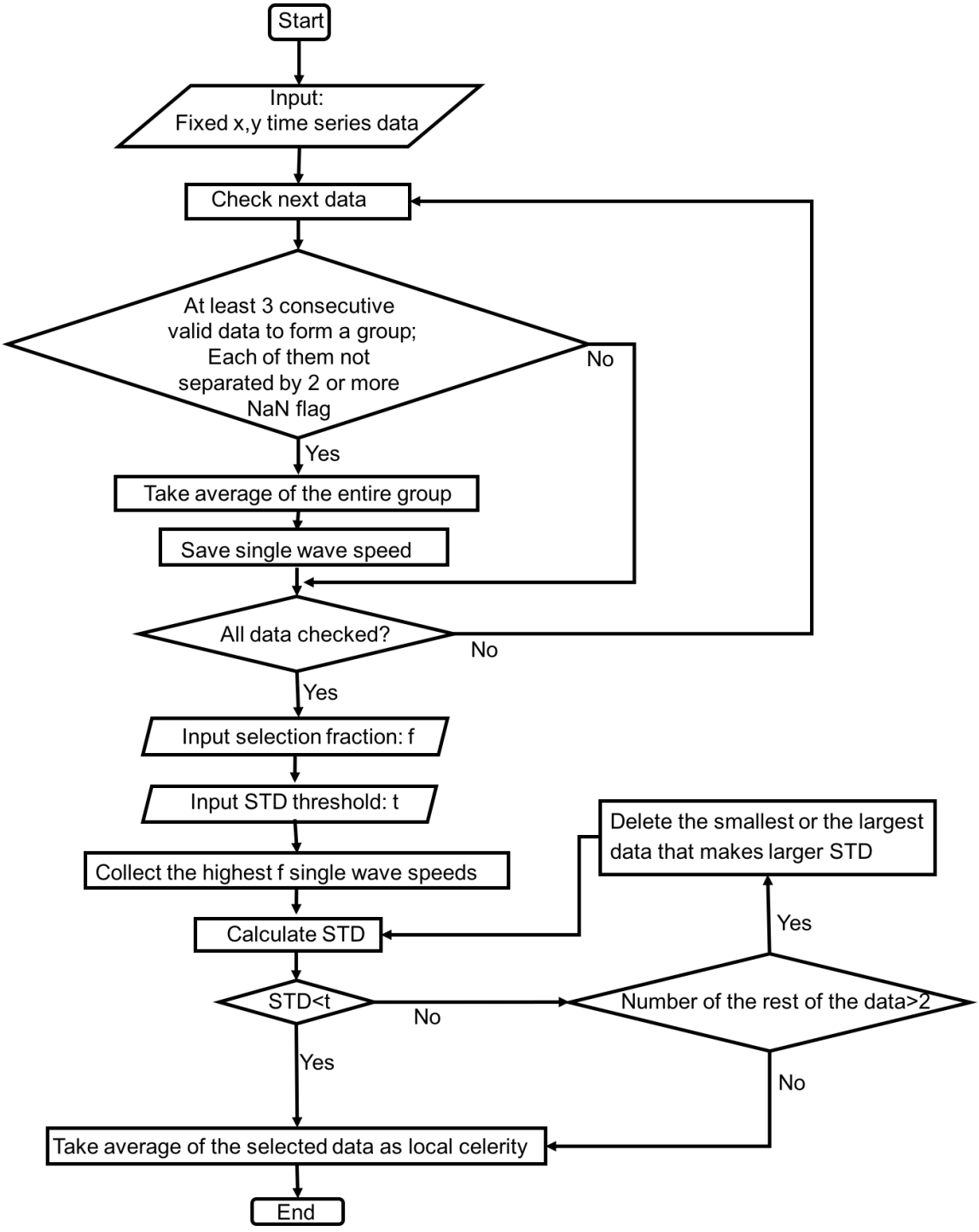

Figure 21. Flow chart for Algorithm I.

The estimation from this method sometimes varied significantly due to the parameter settings. Once again, data from Experiment I was presented to illustrate the variation. The grid point selected was close to the measurement points with known water depth. After inversion, the displacement should be between 5 and 5.5. In Table 5, the results from choosing the highest 1/3 and 1/4 were being compared.

Table 5. Algorithm I results with different portion assigned. Data from Experiment I was used for explanation.

Highest 1/3 Displacements	Highest 1/4 Displacements
7.13	7.13
7.06	7.06
4.99	4.99
4.66	4.66
4.39	—
Mean: 5.65	Mean: 5.96
Result: 4.68	Result: 7.10

Table 5 shows a case using 0.6 as the threshold for standard deviation. When the elimination process began for the 1/3 case, 7.13 was the one farther away from mean and was deleted. The final result was 4.68. On the other hand, for the 1/4 fraction method, the result was 7.10. This example showed how user selection can affect the results. The goal was to examine and select reasonable parameters which lead to accurate data in most grid points. If there are enough good data, the failure calculation may be filtered or smoothed out afterward.

In Algorithm II, a histogram was used to separate the wave speeds by their displacement magnitude. After categorizing, checking started from the bin with the largest speed. When multiple waves were detected in a bin, or when waves appeared in two

consecutive bins, the bin(s) would be selected. The data in the bin(s) were then be averaged to represent the local celerity. Likewise, the reason for doing this was to pick the largest displacement while filtering out the error results.

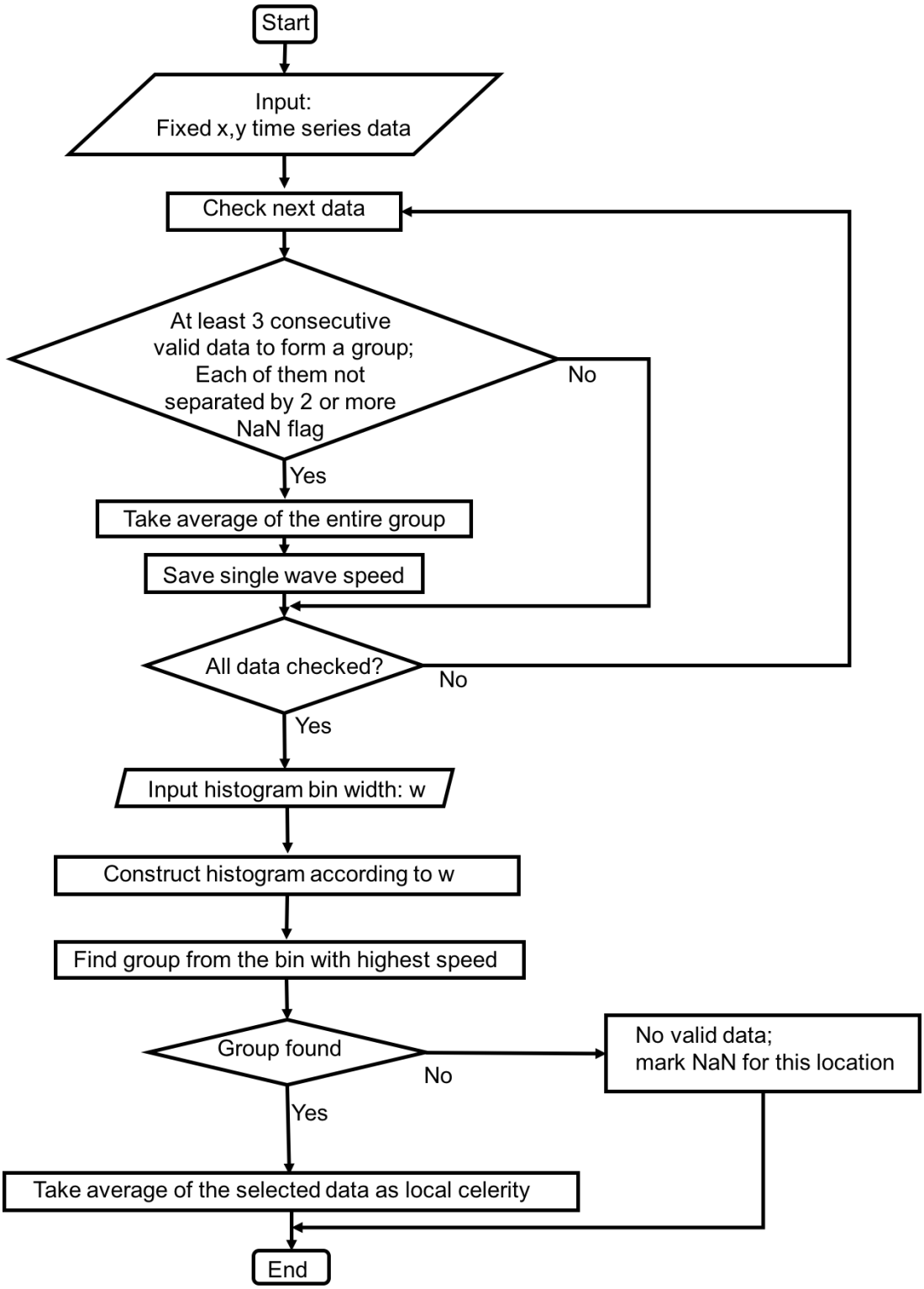

Figure 22. Flow chart for Algorithm II.

Several cases may happen in the histogram selection. With bin width 0.5, two typical cases will be shown.

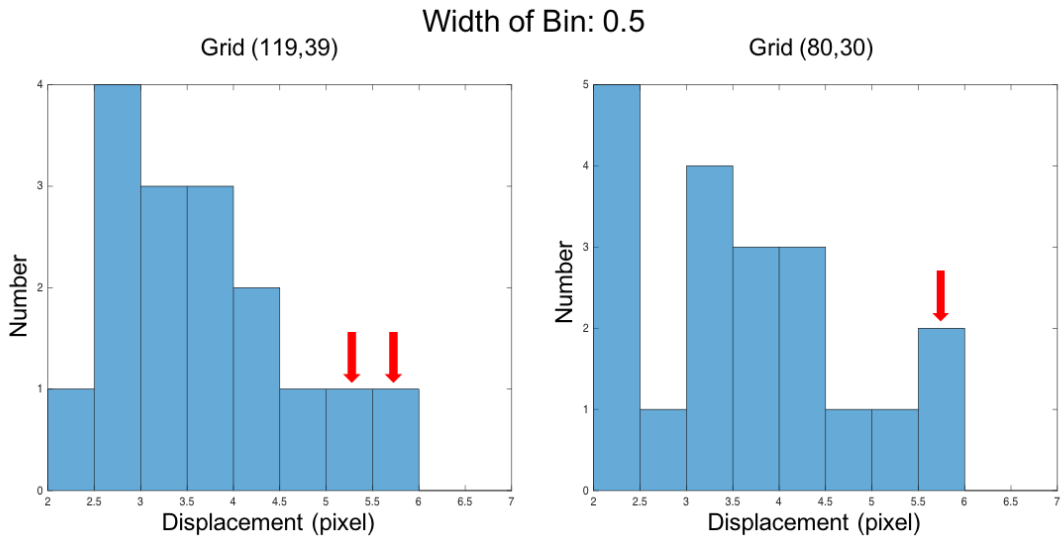

Figure 23. Histogram distribution and selection. Two different selection results using 0.5 bin width. Data in the bins with red arrows pointing at were selected.

The bins with red arrows pointing at them were the ones being selected. The data in the bin were averaged, and they were close to the 5 to 5.5 range as measured. The histogram with bin width reduced to 0.3 will be shown below.

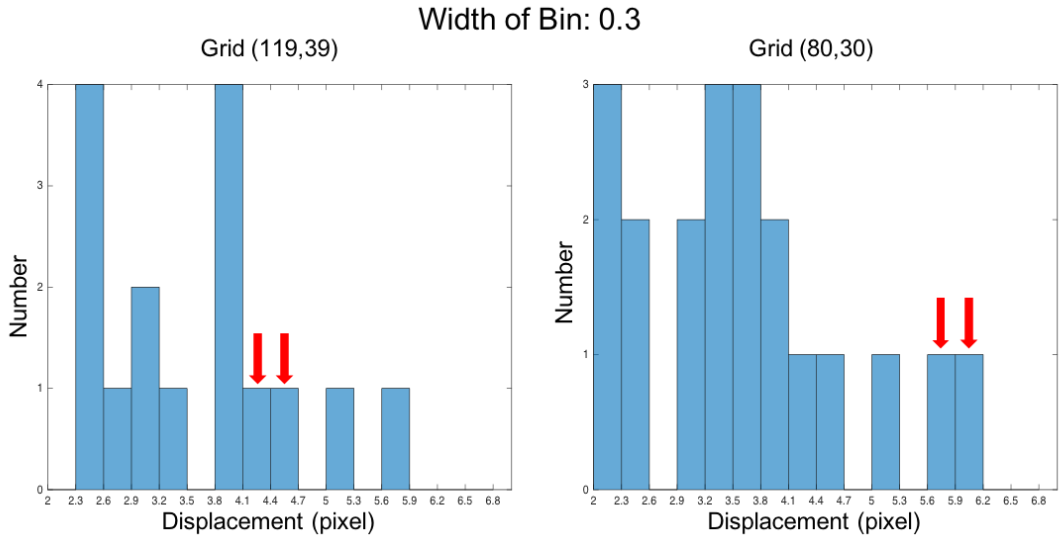

Figure 24. Histogram distribution and selection. Two different selection results using 0.3 bin width. Data in the bins with red arrows pointing at were selected.

Clearly, at grid number (119, 39), the selected value became smaller than the theoretical result. As a result, the bin width determination was a crucial topic. When analyzing a longer video, more frames were being processed, and more waves were detected. With sufficient data collected in the histogram, the selecting threshold can be adjusted accordingly. However, when the bin width was much smaller than the error introduced during the experiment (e.g. drone drifting error), the categorization was ignoring certain data. On the contrary, a bin width larger than the previous error may lead to larger total error. Both algorithms were built assuming more than one desired celerity passed through every interrogation window during the filming.

After extracting the displacement data, they were combined with the pixel-centimeter conversion coefficient and the frame rate to calculate the wave speeds at each grid point. Dispersion relation, Eq. (3), was then used to derive the local water depth. A

median filter was used to delete the stray vectors two times standard deviation away from local mean. The filtering area was a dynamic range from 3×3 to 5×5 which depends on the number of valid data. Also, the PIV error were considered in the process. The larger error between 2 times standard deviation and intrinsic PIV error, defined to be 0.25 pixel, was set as the threshold. The filtering was carried out with modified MATLAB function, vector_filter_median, from open source MPIV [Mori and Chang, 2003]. Assuming the slope was mild, Kriging interpolation was then applied to fill the empty elements. Finally, a 3×3 kernel, $\begin{bmatrix}1 & 2 & 1\\2 & 4 & 2\\1 & 2 & 1\end{bmatrix}$, was used as a low pass filter to smooth out the 50% overlap PIV results. MATLAB scripts used for interpolation and smoothing were also modified based on the ones in MPIV toolbox.

CHAPTER IV

RESULTS AND DISCUSSION

Two sets of experiments were performed, which will be presented as Experiment I and Experiment II. Drone hovering heights were about 50m and 55m accordingly. Experiment I was done in April, 2017, while Experiment II filmed a longer video in July, 2017. Locations are shown in Figure 25.

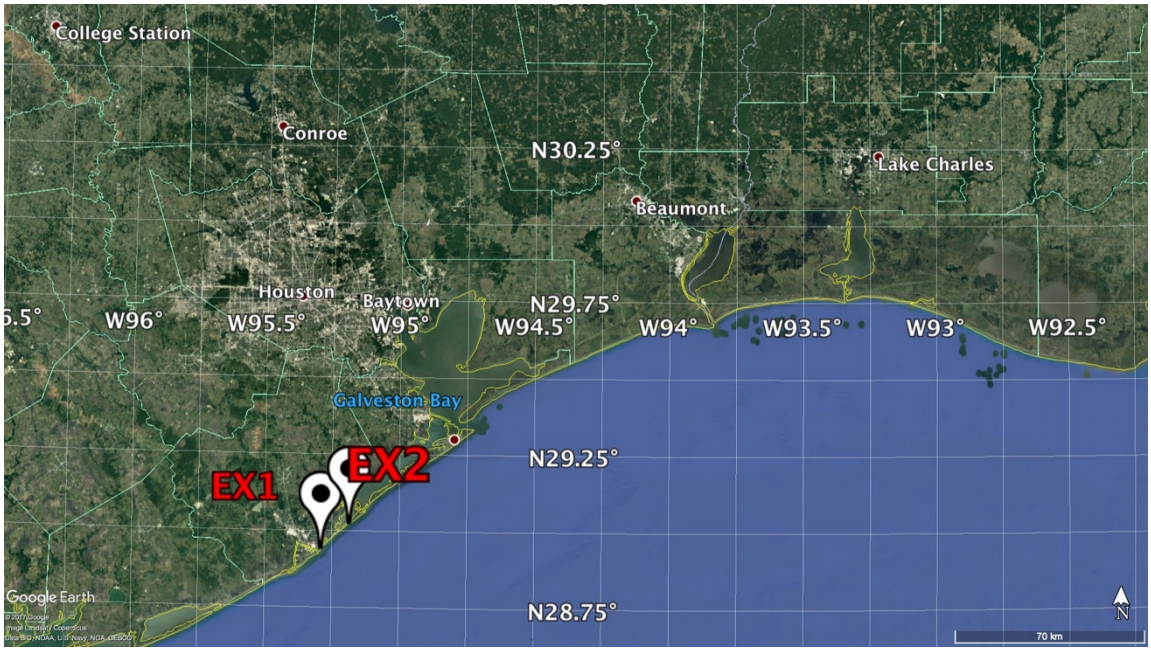

Figure 25. Experiment I and Experiment II location view. Labeled as EX1 and EX2 respectively. Source: 28.75° N and 95.04° W. Google Earth. Viewed 9/7/2017

Both experiments focused on Freeport area in Texas. Waves in the Gulf of Mexico were utilized as the tracer for the PIV analysis and the fundamental material for applying the linear dispersion relation. The natural condition from Surfside Beach all the way north-east till the end of the island looked similar. Consequently, we may expect similar trend

in the results of the two sets of experiments. Instead of sandy beach, riprap along the open ocean was captured in the Experiment I. This was applied to correct the drone drifting effect, and will be further illustrated in Section4.1 More about the experimental condition, settings, and algorithm will be discussed in the following sections.

4.1 Experiment I

Experiment I was done on April 8th, 2017. Local wind speed: 17 mph, SSE. GPS position: 95.2915 N, 28.9427 W. Drone hovered at height between 50.5 to 51.0 m. Camera resolution: 2160 by 4096 pixel, frame rate: 24 FPS. The location will be presented closer in Figure 26, and the filming view has been shown in Figure 12.

Figure 26. Experiment I location view. Drone hovering point labeled as EX1. Source: 28.9427° N and 95.2915° W. Google Earth. 2/15/2016. Viewed 9/7/2017

For a clear view, detailed conditions and the settings are shown in Table 6.

Table 6. Experiment I filming condition and camera settings.

Experiment I	
Hovering Condition	
GPS Position	(28.9427° N , 95.2915° W)
Wind Speed (mph)	SSE 17
Drone Height (m)	50.5-51.0
cm-pixel Conversion Coefficient (cm/pixel)	2.19
Camera Settings	
Resolution (pixel×pixel)	2160×4096
FPS (1/s)	24
Video Length (minute: second)	5:00

The texture of the rocks at the shoreline showed significant brightness difference, which led to intensity difference in image matrices. When the contrast was easily identified, it was an appropriate material to be applied to do PIV analysis. Since the rocks were fixed on the ground, the displacement of the rocks detected between frames was the opposite of the drone motion. Similar technique was explained in Section2.3.2. Drone drifting error was removed by subtracting the displacement of the rocks from the wave front displacement. For example, if the displacement of the rocks was calculated to be 0.5 pixel toward west between frames, and displacement of wave front was 4 pixels toward west, then in the algorithm, 3.5 (4-0.5) pixels toward west would be determined as the corrected wave motion. A user defined MATLAB script was developed to execute the rock displacement calculation. PIV calculated results from a chosen riprap area was collected, and displacements outside 1.5 times standard deviation from mean were deleted in order to get rid of the bad vectors. The stray vectors may be caused by imperfect local

texture. The remaining data were determined as valid displacements, which were used to calculate the average and treated as the rocks displacement between the frames. Figure 27 shows the calculated displacement vectors at grid points in a selected region.

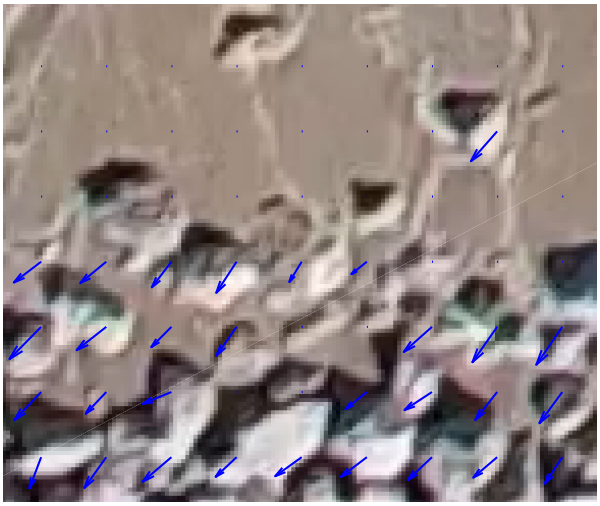

Figure 27. Displacement vectors at selected reference region. Displacement of the fixed rocks will be considered as drone drifting motion.

The displacements at the rock region were close to each other as expected. It was noted that the size of the interrogation window to calculate rocks displacements chosen in DaVis program can be different from the one for calculating wave speed. The selection depends on the size of the rocks. In Experiment I, the wave speeds were calculated using 32×32 window size, while 64×64 was employed for the rocks displacements.

From the five-minute movie, totally 7201 frames were included in the analysis. Algorithm II, explained in Section3.4 was applied. Histogram bin width was set at 0.5. Filtering, interpolating, and smoothing were done. In this case, the median filter did not change the results a lot. Only a few data points were deleted by the median filter. It was noted that in both cases, the data near the image edges were excluded during filtering and

interpolating. Invalid calculation may occur more often at the boundary when processing PIV. Even though the stray vectors were replaced by NaN flags, they may lead to poor condition or bad calculation during the post-processing. Those data near the edge were combined with the center data afterwards. As will be shown in Figure 28, there were more blanks at the top and bottom of the plot representing the NaN elements.

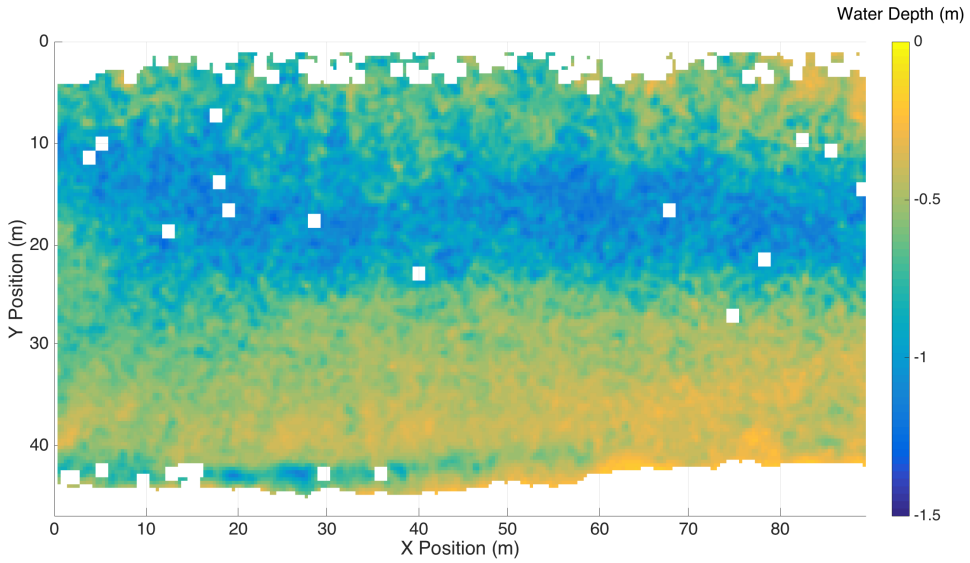

Figure 28. Two dimensional view of Experiment I estimated results with colormap indicating water depth.

Figure 28 shows the two dimensional estimation results with colormap representing local elevation in meter. The orientation is the same as the camera view (Figure 12) where x is long-shore direction and y axis is cross-shore direction.

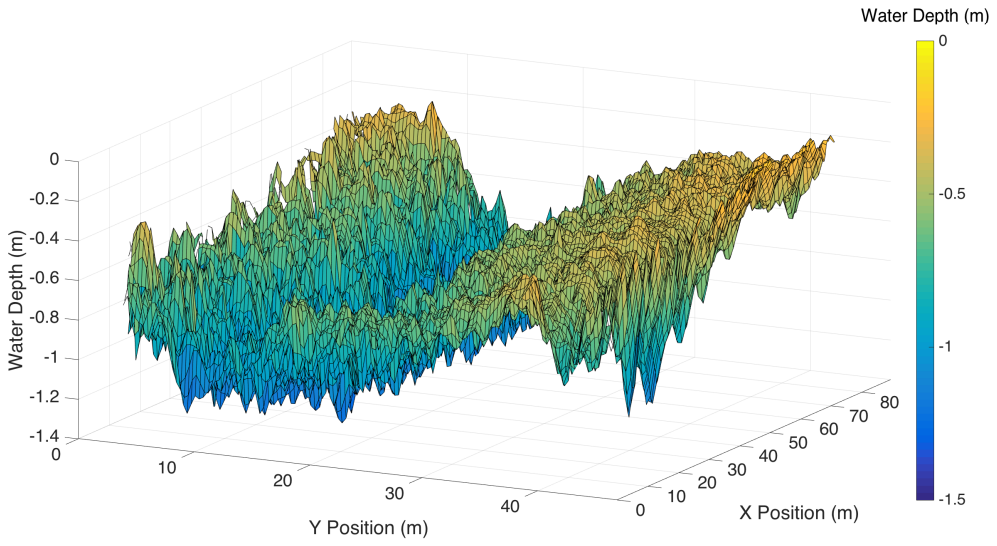

Figure 29. Three dimensional view of Experiment I estimated results in meter.

Figure 29 shows the same estimation in three dimensional view. Colormap and z axis represents local elevation in meter. As pixel-centimeter conversion coefficient 2.19, the surveying region for 2160×4096 resolution camera was approximately $47(\mathrm{m})\times90(\mathrm{m})$. As mentioned in Section3.4, water depth at two locations in the frame were measured, and they will be used here to verify the calculation results. The measurement locations were detected in the video so the pixel number could be extracted. According to the interrogation window size, the pixel number was further converted to the grid number. In Experiment I, the two measurement points were in the $(130,35)$ window and the $(151,35)$ window. The local results are show in Figure 30.

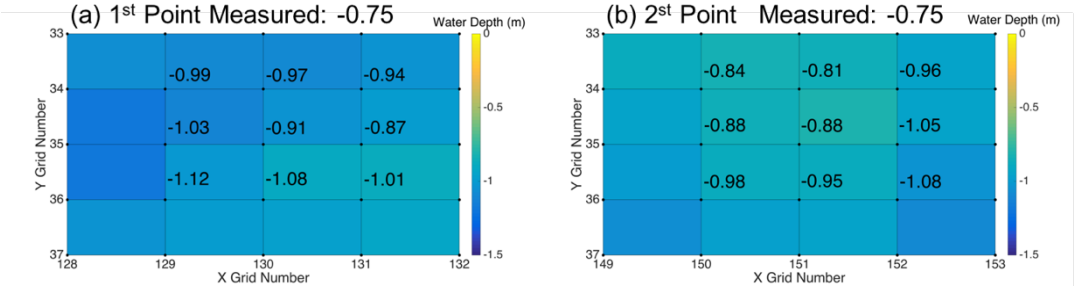

Figure 30. Data of Experiment I validation points and their neighbors. (a) (130, 35) with measurement: 0.75m. (b) (151, 35) with measurement: 0.75m

5×5 square areas with measurement points at the center were shown. The data for the 3×3 grid points at the center were displayed, and were used to calculate the local mean and the local standard deviation. The estimated water depth for the first measurement point was 0.91 (m), local mean was 0.99 (m), with standard deviation 0.09. For the second measurement point, estimation: 0.88 (m), local mean: 0.94 (m), standard deviation: 0.08.

Table 7. Experiment I measured data and estimated data.

	1st Point	2nd Point
Measured Depth (m)	0.75	0.75
Estimated Depth (m)	0.91	0.88
Local Mean (m)	0.99	0.94
Local Standard Deviation (m)	0.09	0.08

From the data, either estimation was larger than the measurement depth. The results at the center points were close to local means, and the local standard deviations are small. Even though the matrix has been smoothed, the stable data still indicated reasonable estimation since mildly changing elevation was assumed.

4.2 Experiment II

With the experience from the previous trials which will be mentioned in Sec4.3 and the histogram distribution from Experiment I, Experiment II was planned in order to examine the result with a longer video. With more waves passing through, a more complete distribution could be expected. Experiment II was carried out on July 10th, 2017. Surveying location is shown in Figure 31, labeled as EX2.

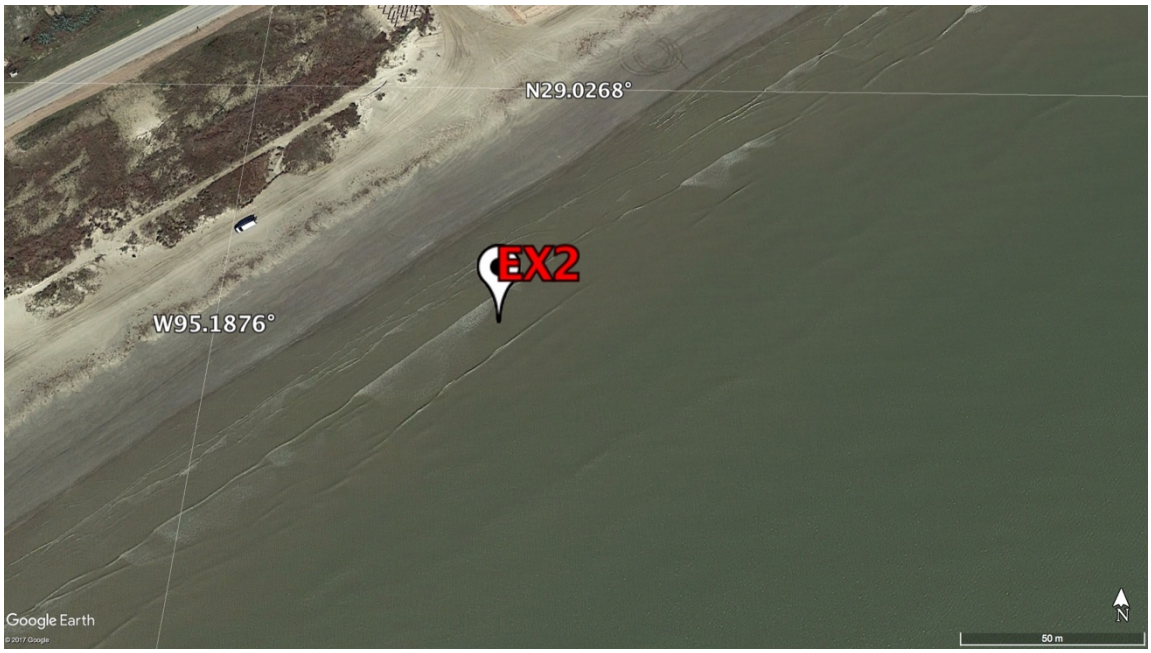

Figure 31. Experiment II location view. Drone hovering point labeled as EX2. Source: 29.0260° N and 95.1867° W. Google Earth. 1/22/2017. Viewed 9/7/2017

More about the conditions and settings are listed in Table 8.

Table 8. Experiment II filming condition and camera settings.

Experiment II	
Hovering Condition	
GPS Position	(29.0260° N , 95.1867° W)
Wind Speed (mph)	SE 7
Drone Height (m)	55.1-55.7
cm-pixel Conversion Coefficient (cm/pixel)	2.40
Camera Settings	
Resolution (pixel×pixel)	2160×4096
FPS (1/s)	24
Video Length (minute: second)	10:45

Below is a frame view showing the filming region. Area about $52(\mathrm{m})\times98(\mathrm{m})$ wide was being surveyed.

Figure 32. View of Experiment II surveying area.

As shown in Figure 32, no fixed structure was recorded in the film. Therefore, this was also a test for an analysis without reference points to remove the drone drifting effect.

Figure 33 shows a random wave breaking area with the calculated displacement vectors superimposed on. Again, the distribution satisfied the assumption in the filtering algorithm.

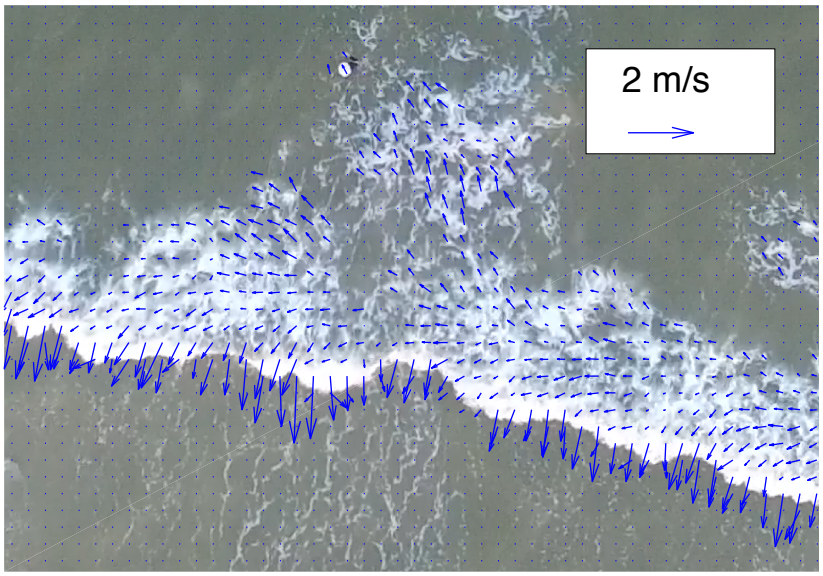

Figure 33. Examination of Experiment II displacement vectors distribution. Calculated displacement at a breaking wave area in a random frame.

Algorithm I was used in Experiment II. The highest 1/5 wave speeds were averaged to represent the desired celerity. With a longer video and 15499 frames analyzed in this case, it was believed that more wave speeds were collected. As a result, the further filtering using standard deviation in Algorithm I was able to delete the stray vectors in most of the grid points. Estimated bathymetry in two dimensional view with colormap is presented in Figure 34 with orientation matching the one in Figure 31.

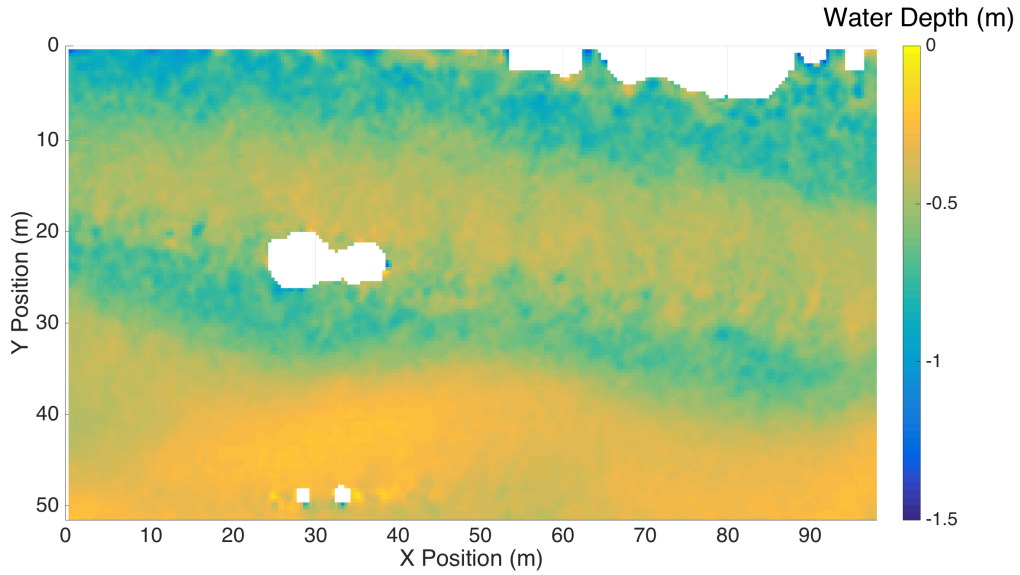

Figure 34. Two dimensional view of Experiment II estimated results with colormap indicating water depth.

Figure 35 shows the three dimensional estimation.

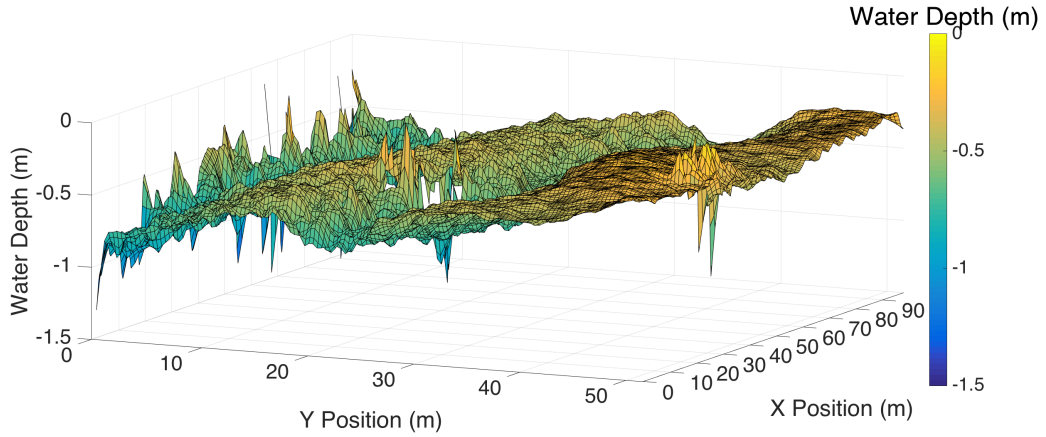

Figure 35. Three dimensional view of Experiment II estimated results in meter.

In Experiment II, three verification points were measured. Once again, the grid points and their neighbors will be presented in Figure 36.

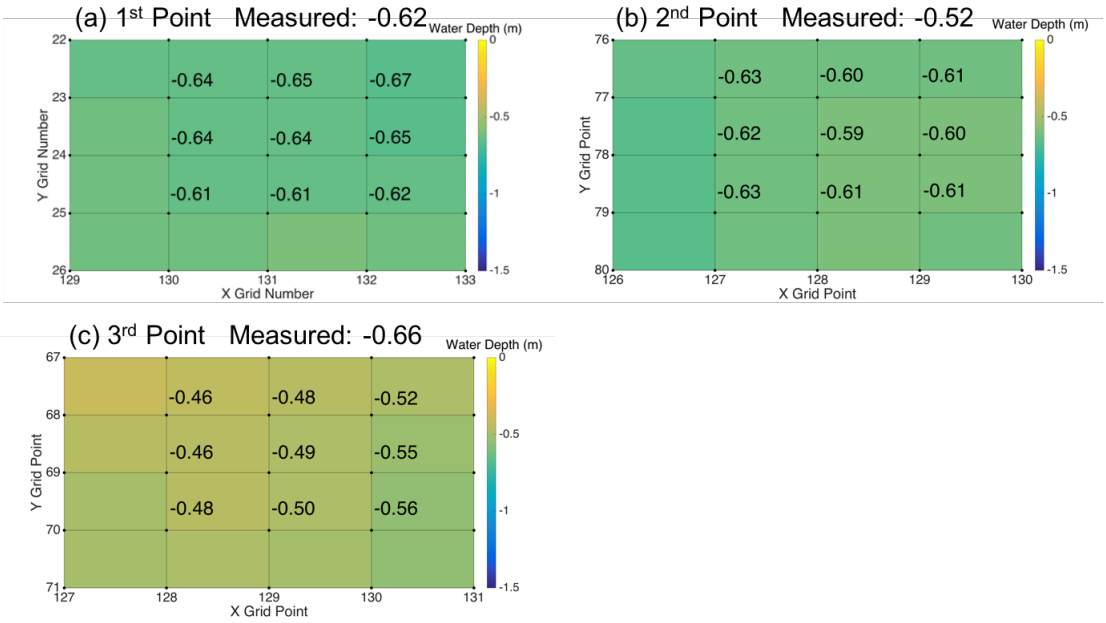

Figure 36. Data of Experiment II validation points and their neighbors. (a) (131, 24) with measurement: 0.62m. (b) (128, 78) with measurement: 0.52m. (c) (129, 69) with measurement: 0.66m.

The comparison of the estimation and measurement are listed in Table 9.

Table 9. Experiment II measured data and estimated data.

	1st Point	2nd Point	3rd Point
Measured Depth (m)	0.62	0.52	0.66
Estimated Depth (m)	0.64	0.59	0.49
Local Mean (m)	0.63	0.62	0.50
Local Standard Deviation (m)	0.04	0.02	0.04

It was obvious that the results of the two points in Experiment I and the first two points in Experiment II were overestimated. However, only the estimation depth for the third point in Experiment II was far smaller than the actual field measurement. According to the performance, it was defined as an outlier. The outliers might be caused by local

topographic event with scale smaller than the wave length. More about the results will be discussed in the following section.

4.3 Discussion & Conclusion

Viewing both projects from a larger scale, the estimated water depth in the offshore direction went deeper gradually and back to a slightly shallower depth. This can be a typical trend with the concave part caused by erosion from breaking waves. In addition, the trend was verified during Experiment II. When walking in the offshore direction with a stick measurement, not only can the observer feel the concavity, random measurement points can also help with verification. Water depth from 0.52m (2^{nd} point), 0.66m (3^{rd} point), to deeper than 0.78m (not included in the video), and back to 0.62m (1^{st} point) were measured. It was noted that even if the third point was replaced by the calculated data, the concavity still existed. In conclusion, the bathymetry estimated shows reasonable trends in either trial.

When closely viewing the data points with measurements, the 3^{rd} point in Experiment II can be excluded as its estimation differs a lot from the other four points. Also, it was the only location being underestimated. As explained in Section2.1, this might be introduced by local bathymetry changing with scale smaller than the order of the wave length, so that the phase speed was not able to reflect the restraint. In this case, the measurement point may be a local "small" scale (compare to wave length) hollow area.

The results of the remaining four points perform similar trends. The overestimations can be explained by the non-linearity and wave breaking effect illustrated in Section2.1. Models in Eq. (6) and Eq. (7) will be applied for correction. Without local wave height measurement, the data from the closest NOAA buoy was used. Station 42019 located at 27.907° N, 95.352° W provides 20-minute measured significant wave heights. In the period when Experiment I and Experiment II were carried out, the significant wave heights were 1.01 and 0.4 respectively. They will be combined with the measured water depth and plug in to Eq. (6) (Correction1). For Eq. (7), the previous review shows a $= 1.3$ may be too large. Consequently, 1.2 (Correction2) and 1.1 (Correction3) will be tested here.

Table 10. Four data points with non-linear effect correction using different models

	Experiment I 1st Point	Experiment I 2nd Point	Experiment II 1st Point	Experiment II 2nd Point
Measured	0.75	0.75	0.62	0.52
Linear Estimation	0.91	0.88	0.64	0.59
Correction1	0.39	0.38	0.32	0.33
Correction2 ($a = 1.2$)	0.63	0.61	0.44	0.41
Correction3 ($a = 1.1$)	0.75	0.73	0.53	0.49

Obviously, Correction1 using Eq. (6) made the adjustment too far. This may be inferred to be caused by the large wave height data. The buoy was located more offshore than the surveying area. Accordingly, larger wave height may be measured, and led to larger a. Checking the results using Correction2 and Correction3, it was found that the influence from a was significant. Rewrite Eq. (7),

$$h = \frac{c}{a^2 \times g} \tag{12}$$

h is inversely proportional to a^2. To consider non-linear effect, determining constant a was a crucial issue in the present study. When the wave just broke, larger a may lead to more accurate corrections. As energy dissipating, a should be decreasing toward the shore line. With $a = 1.1$, Correction3 provides solid results.

The percentage errors for linear estimation and Correction3 were calculated.

Table 11. Percentage errors of four data points with linear estimation and correction model3 (a=1.1)

	Experiment I 1st Point	Experiment I 2nd Point	Experiment II 1st Point	Experiment II 2nd Point
Linear Estimation	+21%	+17%	+3%	+13%
Correction3 (a = 1.1)	0	-3%	-15%	-6%

As mentioned previously, the results were overpredicted without considering the non-linear effect. The average percentage error was +13.5%. After applying correction, the average error decreased to -6%.

The location for Experiment II was selected to be covered in the region with bathymetry data provided by NOAA [Taylor, *et al*. 2008]. However, the data was too coarse to be compared. In NOAA data, the resolution differs with the finest grid about 10 m, while in the present study, Experiment II provides 0.38 m resolution. Obviously, the advantage in resolution for the introduced method was shown.

Besides cases like the 3rd point in Experiment II, where phase speed was not able to present small scale events, other restraints will be discussed. Before Experiment I and

Experiment II were performed, filming projects have been done at a lake (Lake Bryan, Texas), and a bay area (Galveston Bay, Texas). However, they did not work well. In the lake project, the video built by the frames with calculated velocity vectors was examined. When playing the video, the vectors rescaled unstably, which means the estimated wave speed was not continuous. This might be caused by similar color in wave crest and trough. When the intensities were very close, there was a higher chance that the cross correlation be influenced by outliers.

In both the lake and the bay projects, the estimation did not look good with some local extreme values. When checking the velocity vectors superimposing on the images and the videos, they were not smooth and not consistent enough. Besides the poor image quality, the crucial reason of the failure was inferred to be caused by the closed experiment area. With the limited water area, the desired long waves did not form. Most of the waves recorded in the video may be local wind waves or ripples created by ships. Refer to the restriction from wave theory stated in Section2.1, the area of interest was reset to an open beach. At Surfside Beach, Texas, facing the Gulf of Mexico, Experiment I and Experiment II showed reasonable estimation.

Between Experiment I and Experiment II, another experiment has also taken place at the Surfside Beach region. However, only 2.5 minutes were filmed with about 3600 frames, and the water depth was underestimated. In the process and algorithms of the present method, many bad data were collected. They might be filtered out by different thresholds, but still some may stay, influence the smoothing, and affect the result. The solution was to collect more data to make the displacement histogram distribution close

enough to represent actual wave condition. Therefore, it was important that the video was taken long enough to capture enough waves.

CHAPTER V

CONCLUSION

In the present research, nearshore bathymetry was estimated in a convenient way. Low cost and mobility are the main advantages and the purpose to further explore this method. Moreover, the method introduced in the present research can provide much finer resolution in comparison to existing field measurement data. A UAV was utilized to collect imagery. As the technology develops, UAVs and cameras will cost less and provide better quality, leading to better results for estimation. For example, reliable hovering stability and batteries providing longer flying time can be expected. on the other hand, the PIV technique is a well-developed tool applied to analyze data. The extensive application and the thorough result observation have made the principles for parameter settings clear and the uncertainties predictable.

From the field observation, it is believed that the two sets of experiments, Experiment I and Experiment II, successfully provide the trend of the bottom topography. With the linear dispersion relation, the water depth at the grid points were overestimated by different amounts depending on local water depth. Correction can be done to better fit the non-linear effect caused by wave breaking. Excluding the outlier to compare with the local measurement, the average error was 6%.

With low cost and accessible tools, this method can be performed easily; however, still some constraints have to be noted.

- There has to be long waves propagating through the area of interest.

- The video has to be long enough and capture sufficient amounts of long waves passing. Since the current data collection includes all kinds of noise, more "good data" collected will be more likely to result in a precise estimation.

Here are some suggestions that may improve the precision or expand the application in future estimation. Evidently, about the equipment, a UAV with better hovering stability will be able to take more accurate measurements. While it is possible to make correction post hoc as done in Experiment I, it is challenging to various factors. For instance, when image frames do not contain any fixed reference landmark, users will have to retrieve the motion history data from the drone. In addition to horizontal and vertical motion, tilting angle can affect the view as well. Clearly, a reliable UAV will help avoid the complex corrections especially when several thousand frames are needed to be processed.

Another decisive tool is the camera. With larger sensor array, the higher camera resolution covers larger filming area with the same grid point density. With larger frame rate, the wave motion can be detected in more detail especially when the experiment extends further offshore where the water is deeper and the waves travel faster. In the present study, the resolution and the frame rate provided satisfactory results. The property that attracts the researcher's attention is the dynamic range of the camera. The one in the present case is 8-bit, which means from 0 to 255, there are 256 degrees between black and white. If greater dynamic range can be provided by the camera, the detail of the view can be maintained better. In other words, areas that look the same under the 8-bit camera may be different under a camera with greater dynamic range. Since the light scattered by wave

troughs and wave crests are different, the brightness level should be different. When the dynamic resolution is fine enough to detect the difference, the application does not need to be restrained in the breaking zone. Besides the surveying area being expanded, the precision may also be improved when going offshore where the non-linear effects caused by wave breaking does not exist. It was noted that the algorithm used in the present project makes the assumption that the experiments are done in the shallow water conditions.

Since more commercial drones are designed for entertainment usage, the specifications of the cameras that come out of the box may not satisfy the researches. However, thanks to the increasing load that can be carried by UAVs, it is possible to mount a user selected camera on the drone. Furthermore, if other kinds of devices, like thermographic cameras, are connected, extensive application can be expected.

As demonstrated in Section4.3, the correction with Eq. (7) using $a = 1.1$ provides good estimation with 6% error. Without any verification measurements, determining a reasonable value of a would strongly influence the precision of this method. In the present projects, the wave heights observed in the field are not big as researchers can stand still not affected by the waves or the splashing water. From Eq. (6), lower values for a can be expected from small waves. However, this does not provide a systematic way to quantify a. If no measurements are taken, selecting the parameter a is an interesting direction for future work.

REFERENCES

Adrian, R. J., [1988] "Statistical properties of particle image velocimetry measurements in turbulent flow," *Laser Anemometry in Fluid Mechanics (Lisbon: Instituto Superior Tecnico)*, 115–129

Berkhoff, J. C. W. [1973] "Computation of combined refraction—diffraction," *Coastal Engineering 1972*, 471-490.

Berkhoff, J. C. W., N. Booy, and A. C_ Radder. [1982] "Verification of numerical wave propagation models for simple harmonic linear water waves," *Coastal Engineering, 6(3)*, 255-279.

Birkemeier, W. A., and Mason, C. [1984] "The CRAB: A unique nearshore surveying vehicle," *Journal of Surveying Engineering, 110(1)*, 1-7.

Bouguet, J. Y., [2000] "Matlab camera calibration toolbox," *Caltech Technical Report.*

Catálan, P. A., and Haller, M. C., [2008] "Remote sensing of breaking wave phase speeds with application to non-linear depth inversions," *Coastal Engineering, 55(1)*, 93-111.

Chang, K. A., and Liu, P. L. F. [1998] "Velocity, acceleration and vorticity under a breaking wave," *Physics of Fluids, 10(1)*, 327-329.

Chen, C., Beardsley, R. C., and Cowles, G. [2006] "FINITE VOLUME COASTAL OCEAN," *Oceanography, 19(1)*, 78.

Cowen, E. A., Mei Sou, I., Liu, P. L. F., and Raubenheimer, B. [2003] "Particle image velocimetry measurements within a laboratory-generated swash zone," *Journal of Engineering Mechanics, 129(10)*, 1119-1129.

Dugan, J. P., Piotrowski, C. C., and Williams, J. Z. [2001] "Water depth and surface current retrievals from airborne optical measurements of surface gravity wave dispersion," *Journal of Geophysical Research: Oceans 106.C8*, 16903-16915.

Elgar, S., and Guza, R. T. [1985] "Shoaling gravity waves: Comparisons between field observations, linear theory, and a nonlinear model," *Journal of fluid mechanics, 158*, 47-70.

Elhakeem, A. A., Elshorbagy, W., and Chebbi, R. [2007] "Oil spill simulation and validation in the Arabian (Persian) Gulf with special reference to the UAE coast," *Water, air, and soil pollution, 184(1-4)*, 243-254.

Elsinga, G. E., Scarano, F., Wieneke, B., and van Oudheusden, B. W. [2006] "Tomographic particle image velocimetry," *Experiments in fluids, 41(6)*, 933-947.

Ferreira, C. S., Van Kuik, G., Van Bussel, G., and Scarano, F. [2009] "Visualization by PIV of dynamic stall on a vertical axis wind turbine," *Experiments in Fluids, 46(1)*, 97-108.

Google Earth, 28.75° N and 95.04° W. Data SIO, NOAA, U.S. Navy, NGA, GEBCO. Image Landsat/ Copernicus. Viewed 9/7/2017.

Google Earth, 28.9427° N and 95.2915° W. 2/15/2016. Viewed 9/7/2017.

Google Earth, 29.0260° N and 95.1867° W. 1/22/2017. Viewed 9/7/2017.

Grilli, S. T. [1998] "Depth inversion in shallow water based on nonlinear properties of shoaling periodic waves," *Coastal Engineering, 35(3)*, 185-209.

Holland, T. K. [2001] "Application of the linear dispersion relation with respect to depth inversion and remotely sensed imagery," *IEEE Transactions on Geoscience and Remote Sensing, 39(9)*, 2060-2072.

Holman, R. A. [1995] "The interaction of waves, currents and nearshore bathymetry," In *Proceedings Aha Hulikoa Hawaiian Winter Workshop, (Eds) Muller, P. and Henderson, D*, 257-262.

Holman, R. A., and Stanley, J. [2007] "The history and technical capabilities of Argus," *Coastal engineering, 54(6)*, 477-491

Holman, Rob, Plant, N., and Holland, T. [2013] "cBathy: A robust algorithm for estimating nearshore bathymetry," *Journal of Geophysical Research: Oceans 118.5*, 2595-2609.

Huang, H., Dabiri, D., and Gharib, M. [1997] "On errors of digital particle image velocimetry," *Measurement Science and Technology, 8(12)*, 1427.

Keane, R. D., and Adrian, R. J. [1990] "Optimization of particle image velocimeters. I. Double pulsed systems," *Measurement science and technology, 1(11)*, 1202.

Kähler, C. J., Scharnowski, S., and Cierpka, C. [2012] "On the resolution limit of digital particle image velocimetry," *Experiments in fluids, 52(6)*, 1629-1639.

Keane, R. D., and Adrian, R. J. [1992] "Theory of cross-correlation analysis of PIV images," *Applied scientific research, 49(3)*, 191-215.

Lyzenga, D.R., Malinas, N.P. and Tanis, F.J. [2006] "Multispectral bathymetry using a simple physically based algorithm," *IEEE Transactions on Geoscience and Remote Sensing 44*, 2251-59.

Madsen, P. A., Sørensen, O. R., and Schäffer, H. A. [1997] "Surf zone dynamics simulated by a Boussinesq type model. Part I. Model description and cross-shore motion of regular waves." *Coastal Engineering, 32(4)*, 255-287.

Maeda, T., Furumura, T., Sakai, S. I., and Shinohara, M. [2011] "Significant tsunami observed at ocean-bottom pressure gauges during the 2011 off the Pacific coast of Tohoku Earthquake," *Earth, Planets and Space, 63(7)*, 53.

Meinhart, C. D., Wereley, S. T., and Santiago, J. G. [1999] "PIV measurements of a microchannel flow," *Experiments in fluids, 27(5)*, 414-419.

Melville, W. K., and Matusov, P. [2002] "Distribution of breaking waves at the ocean surface," *Nature, 417(6884)*, 58-63.

Mori, N., and Chang, K. A. [2003] "Introduction to MPIV," *User manual and program available online at http://sauron. civil. eng. osaka-cu. ac. jp/~ mori/softwares/mpiv.*

Mount, R. [2005] "Acquisition of Through-water Aerial Survey Images," *Photogrammetric Engineering & Remote Sensing, 71(12)*, 1407-1415.

Polcyn, F. C., Brown, W. L., and Sattinger, I. J. [1970] "The measurement of water depth by remote sensing techniques (No. 8973-26-F)," *MICHIGAN UNIV ANN ARBOR INST OF SCIENCE AND TECHNOLOGY*.

Polcyn, F. C., and Lyzenga, D. R. [1973] "Calculations of water depth from ERTS-MSS data."

Irish, J., and W. Lillycrop [1999] "Scanning laser mapping of the coastal zone: The shoals system," *ISPRS J. Photogramm. Remote Sens.*, *54*(2-3), 123-129.

Raffel, M., Willert, C. E., Wereley, S., and Kompenhans, J. [2013] "Particle image velocimetry: a practical guide," *Springer*.

Ryu, Y., Chang, K. A., and Lim, H. J. [2005] "Use of bubble image velocimetry for measurement of plunging wave impinging on structure and associated greenwater," *Measurement Science and Technology, 16(10)*, 1945.

Sallenger Jr, A. H., Krabill, W. B., Swift, R. N., Brock, J., List, J., *et al*. [2003] "Evaluation of airborne topographic lidar for quantifying beach changes," *Journal of Coastal Research., 19(1)*, 125-133.

Schäffer, H. A., Madsen, P. A., and Deigaard, R. [1993] "A Boussinesq model for waves breaking in shallow water," *Coastal engineering, 20(3-4)*, 185-202.

Sheng, J., Meng, H., and Fox, R. O. [2000] "A large eddy PIV method for turbulence dissipation rate estimation," *Chemical engineering science, 55(20)*, 4423-4434.

Splinter, K. D., and Holman, R. A. [2009] "Bathymetry estimation from single-frame images of nearshore waves," *IEEE Transactions on Geoscience and Remote Sensing 47.9*, 3151-3160.

Stansby, P. K., and Feng, T. [2005] "Kinematics and depth-integrated terms in surf zone waves from laboratory measurement," *Journal of Fluid Mechanics, 529*, 279-310.

Stive, M. J. F. [1980] "Velocity and pressure field of spilling breakers," *Coastal Engineering 1980*, 547-566).

Stockdon, H. F., and Holman, R. A. [2000] "Estimation of wave phase speed and nearshore bathymetry from video imagery," *Journal of Geophysical Research: Oceans, 105(C9)*, 22015-22033.

Stumpf, Richard P., Kristine Holderied, and Mark Sinclair. [2003] "Determination of water depth with high-resolution satellite imagery over variable bottom types," *Limnology and Oceanography 48.1part2,* 547-556.

Svendsen, I. A., and Hansen, J. B. [1977] "Deformation up to breaking of periodic waves on a beach," *Coastal Engineering 1976*, 477-496.

Taylor, L. A., Eakins, B. W., Carignan, K. S., Warnken, R. R., Sazonova, T., and Schoolcraft, D. C. [2008] "Digital elevation model of Galveston, Texas: procedures, data sources and analysis," *National Geophysical Data Center. National Oceanic and Atmospheric Administration Technical Memorandum NESDIS NGDC-12.*

Thornton, E. B., and Guza, R. T. [1982] "Energy saturation and phase speeds measured on a natural beach," *Journal of Geophysical Research: Oceans, 87(C12)*, 9499-9508.

Turner, I. L., Harley, M. D., and Drummond, C. D. [2016] "UAVs for coastal surveying," *Coastal Engineering, 114*, 19-24.

Westerweel, J. [1993] "Digital particle image velocimetry," *Delft University, 17-18*.

Westerweel, J. [1997] "Fundamentals of digital particle image velocimetry," *Measurement science and technology, 8(12)*, 1379-1392.

Westerweel, J. [2008] "On velocity gradients in PIV interrogation," *Experiments in Fluids*, 44(5), 831-842.

White, D. J., Take, W. A., and Bolton, M. D. [2001] "Measuring soil deformation in geotechnical models using digital images and PIV analysis," *10th International Conference on Computer Methods and Advances in Geomechanics No. 1*, 997-1002.

Willert, C. E., and Gharib, M. [1991] "Digital particle image velocimetry," *Experiments in fluids, 10(4)*, 181-193.

Williams, W. W. [1947] "The determination of gradients on enemy-held beaches," *The Geographical Journal, 109(1/3)*, 76-90.

Zhang, Z. [1999] “Flexible camera calibration by viewing a plane from unknown orientations,” *Computer Vision, 1999. The Proceedings of the Seventh IEEE International Conference on (Vol. 1, pp. 666-673). IEEE*.